

RXTE Spectral Observations of the 1996–97 Outburst of the Microquasar GRO J1655–40

Gregory J. Sobczak

Astronomy Dept., Harvard University, 60 Garden St., Cambridge, MA 02138;
gsobczak@cfa.harvard.edu

Jeffrey E. McClintock

Harvard-Smithsonian Center for Astrophysics, 60 Garden St., Cambridge, MA 02138;
jem@cfa.harvard.edu

Ronald A. Remillard

Center for Space Research, MIT, Cambridge, MA 02139; rr@space.mit.edu

Charles D. Bailyn

Department of Astronomy, Yale University, P. O. Box 208101, New Haven, CT 06520;
bailyn@astro.yale.edu

Jerome A. Orosz

Dept. of Astronomy and Astrophysics, The Pennsylvania State University, 525 Davey
Laboratory, University Park, PA 16802; orosz@astro.psu.edu

Received _____; accepted _____

ABSTRACT

Excellent coverage of the entire 16-month 1996–97 outburst cycle of GRO J1655–40 was provided by the *Rossi X-ray Timing Explorer*. We present a full spectral analysis of these data, which includes 52 Proportional Counter Array spectra from 2.5–20 keV and High Energy X-ray Timing Explorer spectra above 20 keV. We also include a nearly continuous All-Sky Monitor light curve with several intensity measurements per day. The source exhibits two principal outburst states which we associate with the very high and the high/soft states. During the very high state, the spectrum is often dominated by a power-law component with $\alpha = 2.3\text{--}2.7$. The source exhibits intense hard flares which are correlated with changes in both the temperature and radius of the inner accretion disk on time scales of hours to days. During the high/soft state, the spectrum is dominated by the soft thermal emission from the accretion disk with approximately constant inner disk radius and temperature. The power-law component is relatively weak with $\alpha \sim 2\text{--}3$. During the last few observations, the source undergoes a transition to the low/hard state.

The principal discovery of this work is the tight relationship that exists between the inner radius of the disk and the flux in the power-law component. The inner radius is typically $\sim 5\text{--}7 r_g$ ($r_g = GM/c^2 = 10.4$ km for GRO J1655–40). However, during intense hard flares, the inner radius is observed to decrease by as much as a factor of 3 (to $1.6 r_g$) on a time scale of days. This rapid contraction of the inner disk is consistent with the expected effects of radiation drag coupled with changes in the mass accretion rate. The correlation between the inner disk radius and power-law flux suggests that the physical mechanism responsible for producing the power-law emission is linked to the inner disk region.

We find that the 300 Hz QPO (Remillard et al. 1998) is present over a range of inner disk radii (1.6–5.0 r_g); therefore it cannot be due to the precession frequency of the inner disk at the last stable orbit. We confirm that GRO J1655–40 contains a rapidly rotating black hole with $a_* > 0.9$, based on our minimum value of the inner radius. We also find that the 14–28 Hz QPO frequency decreases as the inner disk moves inward, which is contrary to the behavior expected if the QPO were tied to the Keplerian frequency at the shrinking inner edge of the disk.

Subject headings: black hole physics — stars: individual(GRO J1655–40) — X-rays: stars

1. Introduction

The X-ray Nova GRO J1655–40 was discovered 1994 July 27 (UT) by the Burst and Transient Source Experiment (BATSE) onboard the *Compton Gamma Ray Observatory* (Zhang et al. 1994). The optical counterpart was discovered soon thereafter by Bailyn et al. (1995). It was subsequently found that GRO J1655–40 contained a black hole primary with mass $7.02 \pm 0.22 M_{\odot}$ (Orosz & Bailyn 1997; van der Hooft et al. 1998), the most accurately measured mass for any black hole candidate. GRO J1655–40 is one of only eight Black Hole X-ray Novae (BHXN) with a dynamically determined primary mass that exceeds $3 M_{\odot}$, the maximum mass of a neutron star (Kalogera & Baym 1996; McClintock 1998). GRO J1655–40 is one of a few Galactic X-ray sources known to produce superluminal radio jets (Tingay et al. 1995; Hjellming & Rupen 1995). The others are GRS 1915+105, which is also suspected of being a black hole (Mirabel & Rodriguez 1994, 1998), and possibly Cyg X-3 (Mioduszewski et al. 1997; Newell et al. 1998). These sources, and a few other Galactic X-ray sources that exhibit double-lobed radio structures (e.g. 1E1740.7–2942; see Smith et al. 1997 and references therein), are known collectively as the ‘microquasars’, since they have properties analogous to radio-loud active galactic nuclei. GRO J1655–40 is also of intense current interest because it is believed to be a rapidly rotating Kerr black hole based on its spectral characteristics (Zhang, Cui, & Chen 1997a) and on the frame dragging model for the observed 300 Hz QPO (Cui, Zhang, & Chen 1998).

The X-ray behavior of BHXN can be described in terms of five distinct, canonical spectral states characterized by the presence or absence of a soft blackbody component at ~ 1 keV and the properties of a power-law component at higher energies above ~ 10 keV. In order of increasing luminosity, these states are the *quiescent/off*, *low/hard*, *intermediate*, *high/soft*, and *very high* states. The *quiescent/off* state is characterized by an X-ray luminosity several orders of magnitude lower than the other states, and a power-law

spectrum with a photon index ~ 2 (Narayan, Barret & McClintock 1997). The *low/hard* state consists of a power-law component with photon index $\alpha \sim 1.4\text{--}1.9$ with an exponential cutoff ~ 100 keV and a weak thermal component. The *high/soft* state is dominated by a soft ~ 1 keV blackbody component due to a hot accretion disk (Tanaka & Shibasaki 1996) and a power-law with $\alpha \sim 2.2\text{--}2.7$. The *high/soft* state has an X-ray luminosity $L_x \sim 0.2\text{--}0.3 L_{Edd}$ compared to $L_x \lesssim 0.1 L_{Edd}$ for the *low/hard* state (Nowak 1995). The *intermediate* state, as evidenced by its name, has properties in common with both the *low/hard* and *high/soft* spectral states. The intermediate state has been observed as a distinct spectral state in Nova Muscae 1991 (Ebisawa et al. 1994), Cyg X-1 (Belloni et al. 1996), and GX 339–4 (Mendez & van der Klis 1997). The *very high* state spectrum has a dominant power-law component with photon index ~ 2.5 and exhibits strong variability and high X-ray luminosity, $L_x \sim L_{Edd}$ (Ebisawa et al. 1994). Thermal emission from the disk remains visible in the very high state.

In this paper we present the spectral results for 52 pointed observations which cover the entire 16-month 1996–97 outburst of GRO J1655–40 and employed all the instruments aboard the *Rossi X-ray Timing Explorer* (RXTE): namely, the All-Sky Monitor (ASM), the Proportional Counter Array (PCA), and the High Energy X-ray Timing Experiment (HEXTE). Our results consist of ASM lightcurves, 52 detailed PCA spectra from 2.5–20 keV, and HEXTE spectra above 20 keV when the hard X-ray count rate was sufficient. The spectra were fit to a model including interstellar absorption, multicolor disk blackbody, and power-law components. A timing study based on these same RXTE observations of GRO J1655–40 is presented in a companion paper (Remillard et al. 1998).

The observations are discussed in § 2, and the results of the spectral fitting are presented in § 3. Section 4 highlights the correlations between the disk and power-law components. Section 5 contains a discussion of corrections to the observed spectral

parameters due to general relativistic effects and an estimate of the black hole angular momentum. In § 6 a comparison is made between GRO J1655–40 and GRS 1915+105, which also exhibits power-law flares associated with changes in the temperature and radius of the inner accretion disk. In § 7 we present a model which relates the changes in the inner disk radius observed in GRO J1655–40 to the effects of radiation drag forces in the inner disk and changes in the mass accretion rate. GRO J1655–40 is compared to Nova Muscae 1991 (GRS 1124–683) and the ADAF (Advection Dominated Accretion Flow) model is used to interpret a spectral anomaly in § 8. The relation between the observed spectral parameters and QPOs is discussed in the final section followed by a brief summary of our results.

The units used in this paper are $r = R/r_g$ where $r_g = GM/c^2$, $m = M/M_\odot$, $l = L/L_{Edd}$ where $L_{Edd} = 1.25 \times 10^{38} m \text{ erg s}^{-1}$ is the Eddington luminosity, and $\dot{m} = \dot{M}/\dot{M}_{Edd}$, where $\dot{M}_{Edd} = L_{Edd}/(0.1c^2) = 1.39 \times 10^{18} m \text{ g s}^{-1}$ is the Eddington accretion rate, assuming an accretion efficiency of 10%.

2. Observations & Reductions

We present observations covering the entire 16 month 1996–97 outburst of GRO J1655–40 obtained using the ASM, PCA, and HEXTE instruments onboard RXTE. The ASM has three energy channels corresponding to 1.5–3 keV, 3–5 keV, and 5–12 keV (Levine et al. 1996). The PCA data were taken in the “Standard 2” format which corresponds to 129 energy channels from 0–100 keV. The PCA contains five individual proportional counter units (PCUs 0–4). The response matrix for each PCU was obtained from the 1997 October 2 distribution of response files from Keith Jahoda’s ftp site on lheafftp.gsfc.nasa.gov in the subdirectory /pub/keith. Specifically, we used the set p0_63_std2_e3 through p4_63_std2_e3.

The spectrum from each PCU was fit individually over the energy range 2.5–20 keV, including a systematic error in the count rates of 1.5%. The good energy range was decided by trial-and-error fitting of archival observations of the Crab Nebula (1997 July 26 & 1997 March 22) and the data set presented here. The lower limit of 2.5 keV was used because of uncertainty in the response at lower energies, and the upper limit of 20 keV was used because there are systematic problems in the response matrices and background subtraction near 25 keV. The PCA spectra were background subtracted using the standard background models, which include corrections for the instantaneous particle flux, activation, and the cosmic X-ray background. We found that PCUs 2 & 3 yielded reduced chi-squared (χ^2_ν) values consistently higher than PCUs 0, 1, & 4 for fits to archival observations of the Crab Nebula. In addition, we found that PCU 4 gave consistently lower count rates ($\sim 3\%$) than PCUs 0 & 1 at low energies ($\lesssim 6$ keV). Consequently, only PCUs 0 & 1 were used for the spectral fitting reported here and both PCUs were fit simultaneously using XSPEC.

The standard HEXTE reduction software was used for the extraction of the HEXTE data. We used the HEXTE response matrices released 1997 March 20. Only the data above 20 keV was used because of uncertainty in the response at lower energies. The HEXTE modules were alternately pointed every 32 s at source and background positions, allowing background subtraction with high sensitivity to time variations in the particle flux at different positions in the spacecraft orbit. The HEXTE normalization is allowed to float independent of the PCA normalization since there is a $\sim 20\%$ systematic offset between the two instruments in the normalization for the Crab nebula, part of which is due to uncertainties in the deadtime for the HEXTE instrument. All of the normalizations reported here were obtained from the PCA data.

3. Analysis & Results

The total ASM lightcurve (2–12 keV) and the ratio of the ASM count rates (5–12 keV)/(3–5 keV) for GRO J1655–40 are plotted in Figures 1a & b. The origin of time was chosen such that day zero corresponds to the initial rise in the X-ray intensity in the ASM: MJD 50198 = 1996 April 25 (UT) (Orosz et al. 1997). The lightcurve exhibits erratic flaring from approximately day 27 to 147 (MJD 50198+; MJD = JD – 2,400,000.5) and again from day 175 to day \sim 200. The flaring ceases shortly before the gap in the data around day 220, which is when the source moved into the solar exclusion zone (SEZ). The (5–12 keV)/(3–5 keV) ratio is roughly constant following passage through the SEZ, except for a dip followed by a sharp rise near day 470. After the sharp rise, the PCA data show (see below) that the source enters the low/hard state; it is then too faint to detect with the ASM. The outburst of GRO J1655–40 evolves through a succession of three of the canonical spectral states, as indicated in Figure 1a. The states are defined by the behavior of the light curve and the spectral characteristics of each state. Sample spectra from each of these states are plotted in Figure 2, along with the best fit models for each spectrum.

The PCA/HEXTE spectral data were fit using XSPEC to a model of interstellar absorption using the Wisconsin cross-sections (Morrison & McCammon 1983) plus a multicolor blackbody accretion disk (Mitsuda et al. 1984; Makishima et al. 1986) plus a power-law component. In addition, a smeared Fe absorption edge or a Compton reflection component were applied in particular cases, as described below. The hydrogen column density was fixed at 0.89×10^{22} atoms per cm^{-2} (Zhang et al. 1997b).

The four principle quantities returned from the fits were the power-law photon index (α), the power-law normalization (K) in units of $\text{photons s}^{-1} \text{cm}^{-2} \text{keV}^{-1}$ at 1 keV, the color temperature of the inner accretion disk (T_{col}) in keV, and the multicolor disk normalization

parameter:

$$\left(\frac{R_{col}}{km}\right)^2 / \left(\frac{D}{10 \text{ kpc}}\right)^2 \cos \theta, \quad (1)$$

where R_{col} is the inner disk radius in kilometers derived from the color temperature, D is the distance to the source in kiloparsecs, and θ is the inclination angle of the system. The mass, inclination angle, and distance of GRO J1655–40 are well determined: $M = 7.02 \pm 0.22 M_{\odot}$, $\theta = 69.5 \pm 0.1$ (Orosz & Bailyn 1997), and $D = 3.2 \pm 0.2$ kpc (Hjellming & Rupen 1995). Substituting these values into equation (1) allows us to solve for R_{col} in units of $r_{col} = R_{col}/r_g$ where $r_g = GM/c^2 = 10.4$ km.

T_{col} & r_{col} , which are usually referred to in the literature as T_{in} & r_{in} , are often taken to be the temperature and radius of the inner accretion disk. However, corrections for spectral hardening must be made to the observed spectral parameters (T_{col} & r_{col}) to determine the effective temperature and radius of the inner disk (T_{eff} & r_{eff}). These corrections compensate for the fact that electron scattering dominates over absorption as a source of opacity in the disk and affects the inner disk spectrum through Comptonization of the emergent spectrum (Shakura & Sunyaev 1973). Such a Comptonized spectrum may be approximated by a diluted blackbody (Ebisawa et al. 1994):

$$I(E) = \left(\frac{1}{f^4}\right) B(T_{col}, E), \quad (2)$$

where $B(T_{col}, E)$ is the Planck function, T_{col} is the color temperature, and f is the color correction or spectral hardening factor. In this diluted blackbody spectrum, the spectral shape is the same as a blackbody with temperature $T_{col} = fT_{eff}$, where T_{eff} is the effective temperature, and the normalization is smaller by the factor $(1/f^4)$. Since the normalization fit by the multicolor disk model is proportional to r_{col}^2 (see Eq. (1)), the actual radius should be f^2 times larger than obtained from fitting the multicolor disk model. Shimura & Takahara (1995) have shown that the spectral hardening factor $f = (T_{col}/T_{eff})$ can be approximated by a constant $f = 1.7 \pm 0.2$ for $\alpha_v \sim 0.1$, $1.4 \leq m \leq 10$, and $0.1 \leq \dot{m} \leq 10$,

where α_v is the Shakura-Sunyaev viscosity parameter.

Therefore, the fit values of T_{col} and r_{col} can be corrected approximately for spectral hardening by using the following formulas:

$$T_{eff} = \frac{T_{col}}{f} = \frac{T_{col}}{1.7}, \quad (3)$$

$$r_{eff} = f^2 r_{col} = 2.9 r_{col}, \quad (4)$$

where T_{eff} and r_{eff} are the effective temperature and radius of the inner accretion disk. The model parameters, corrected for spectral hardening, are listed in Table 1 and presented in Figures 3a–d. As discussed in § 5, when the inner disk radius (r_{eff}) is close to the last stable orbit around an accreting black hole, there are also general relativistic effects that must be considered. Zhang et al. (1997a) show that such corrections are close to unity for the range of parameters relevant to this paper.

3.1. Very High State

In Figures 1a & 3d, we see that between days 27 and 147 and days 175 and 222, there are sudden flares during which the power-law normalization increases by a factor of ten over only a few days. These flares in the hard component are accompanied by an increase in T_{eff} from ~ 0.76 keV to 1.13 keV (Fig. 3a) and a decrease in r_{eff} from ~ 5.5 to 1.6 (Fig. 3b). There is also an abrupt increase in α from ~ 2.3 to 2.7 (Fig. 3c). We identify this flaring behavior with the very high state. Figure 2a shows an example of the spectrum during the flares. Between days 147 and 175 the power-law (hard) flares cease and the photon index decreases to 2.0–2.2. During this time, the temperature and radius of the inner disk become steady at $T_{eff} \sim 0.75$ keV and $r_{eff} \sim 5.5$; Figure 2b shows a representative spectrum.

For four observations during the hard flares (days 98, 126, and 191 A & B), the fits were significantly improved by adding a Compton reflection component. The Compton reflection

component was calculated using the ‘pexriv’ model in XSPEC version 10 (Magdziarz & Zdziarski 1995). The resulting values of the disk blackbody and power-law parameters did not change significantly, and were independent of the temperature of the reflecting medium. A 6.4 keV iron $K\alpha$ emission line is frequently included with the Compton reflection component in such calculations; however, there was no evidence for 6.4 keV iron $K\alpha$ emission in our spectra. The Compton reflection parameters returned from ‘pexriv’ for the four relevant observations are listed in Table 2.

3.2. High/Soft and Low/Hard States

When the source became observable again after passage through the solar exclusion zone, the power-law normalization had decreased by an order of magnitude relative to the peak values and was typically $\lesssim 5$ photons $\text{s}^{-1} \text{cm}^{-2} \text{keV}^{-1}$ at 1 keV (Fig. 3d). The dramatic hard flares had ceased and the color temperature and radius of the inner disk had settled down to ~ 0.7 keV and $6.5r_g$ respectively (Fig. 3a & b). The photon index varied significantly from ~ 2 to 3 over only a few days (Fig. 3c). We identify this period with the high/soft state. A sample high/soft state spectrum is shown in Figure 2c.

Our initial fits for the high/soft state data were poor ($\chi^2_\nu \sim 1\text{--}4$); however, they were significantly improved by the addition of a smeared Fe absorption edge at 8.0 keV (above the neutral Fe K edge at 7.1 keV) using the ‘smedge’ model in XSPEC (Ebisawa et al. 1994). Figures 4a–c show the effect of the absorption edge on the ratio data/model for a representative high/soft state spectrum. From Figures 4a–c, it is apparent that the addition of an Fe absorption edge significantly improves the χ^2_ν from 1.44 to 1.04 for an edge at 8.0 keV. The best fit edge energy varied from 7 to 9 keV for different spectra. For consistency the edge was fixed at 8.0 keV with a width of 7 keV and only the Fe optical depth was allowed to float. The presence of an Fe absorption feature in BHXR spectra is

well established (e.g. Inoue 1991; Ebisawa et al. 1994).

The disk temperature during the high/soft state is approximately constant from days 307 to 364, then there is a slight increase of T_{eff} from 0.67 keV to 0.71 keV over 28 days from days 364 to 398 (Fig. 3a). After this slight rise, T_{eff} decreases from 0.71 keV to 0.60 keV over the next 47 days (Fig. 3a) and r_{eff} increases from 6.3 to 7.1 (Fig. 3b). On day 455, the disk temperature begins to drop rapidly and decreases from 0.57 keV to 0.26 keV over the final 32 days.

By day 476 the multicolor disk blackbody appears only as a soft excess below 5 keV. The spectra at this time are characteristic of the low/hard state. A representative spectrum is presented in Figure 2e. In the last three observations, the inner disk radius appears to decrease, which is probably due to the failure of the multicolor disk model to adequately describe the system after day 465. Similar behavior was observed in Nova Muscae 1991 (Ebisawa et al. 1994) during the soft-to-hard transition at late times and is discussed in § 8.

The values of α and K for days 14–17 are off the scale used in Figure 3, but are given in Table 1. In this initial group of observations, the spectrum is dominated by a soft thermal component below ~ 10 keV with $T_{eff} \sim 0.7$ keV and by a steep quasi-power-law component with $\alpha \sim 6$ at higher energies. Since the power-law contributes so little flux above 5 keV, compared to the thermal component, we identify these observations with the high/soft state. A sample spectrum from this period is shown in Figure 2d. The quality of the 2.5–20 keV spectral fits was poor ($\chi^2_\nu \sim 5$ –8) during this time. *These spectra resisted all attempts to apply the multicolor disk plus power-law model, including modifications for variable N_H , emission lines, absorption edges, Compton reflection, thermal comptonization, and an exponentially cutoff power-law.* The same difficulty was encountered for six other observations during the high/soft state. As a result, we were forced to fit these spectra using interstellar absorption plus a multicolor disk over the restricted range 2.5–10 keV, and then

fix these parameters when fitting the high/soft energy component with a power-law from 15–20 keV. This approach gave satisfactory values of χ^2_ν (see Table 1). Figure 2d shows a sample spectrum along with the best fit multicolor disk model for these poorly-fit high/soft state spectra. In Figures 3a–d, the spectra which are not well fit by the multicolor disk blackbody plus power-law model above 10 keV are indicated by open circles; in Table 1 the corresponding entries are flagged by footnotes f and g. Note that the derived temperatures and inner disk radii of these cases are consistent with those of the ‘normal’ high/soft state spectra (Fig. 3a & b).

3.3. Disk and Power-law Component Fluxes and Source Luminosity

Figures 5a–c are plots of the total unabsorbed flux (Fig. 5a), the unabsorbed bolometric flux from the disk blackbody component (Fig. 5b) and the unabsorbed flux from the power-law component (2–100 keV) (Fig. 5c). Figure 5d shows the ratio of the disk blackbody to the total flux. During the flares, the power-law component dominates the spectrum and we see that the increase in the power-law flux (Fig. 5c) is accompanied by a decrease in the flux from the disk (Fig. 5b). When the source moves out of the solar exclusion zone, the power-law flux is less than 5×10^{-9} erg s^{−1} cm^{−2} and the flux from the disk component dominates the spectrum. This behavior is even more apparent in Figure 5d, where the disk flux is plotted as a fraction of the total unabsorbed flux from 2–100 keV. During the hard flares, the power-law dominates the unabsorbed flux, contributing $\sim 70\%$ of the total flux (Fig. 5d). During the calm period (around day 160) between the two flaring episodes, the power-law contributes less than 20% of the flux (Fig. 5d). After passage through the SEZ, the disk emission dominates, contributing around 90% of the total flux (Fig. 5d). After day 465, the power-law again dominates the unabsorbed flux, contributing $\sim 70\%$ of the total (Fig. 5d), indicating that the system has undergone a soft-to-hard transition.

Figure 6 shows the 2–12 keV luminosity (which contains a mixture of thermal and power-law components) and the 20–100 keV luminosity in Eddington units for GRO J1655–40, for comparison to Figure 12a in Esin, McClintock, & Narayan (1997a) for Nova Muscae 1991. During the flares, the photon index is ~ 2.5 (Fig. 3c) and the 20–100 keV luminosity is an order of magnitude larger than that of the high/soft state (i.e. for observations after day 252). The flaring episodes are consistent with the very high state. After passage through the SEZ, the 2–12 keV emission is strong and the photon index is generally near 2.5 (Fig. 3c). This period is consistent with the high/soft state. Following day 465, the source fades rapidly, the power-law component hardens, and the fluxes in the hard and soft bands become comparable, as the source enters the low/hard state.

4. Correlations in the Disk and Power-Law Parameters

Figures 3a & b show that during the flares, T_{eff} increases from ~ 0.76 to 1.13 keV, while r_{eff} decreases by a factor of about three from ~ 5.5 to 1.6. Figure 7a shows the correlation between T_{eff} and r_{eff} , from which it is apparent that T_{eff} increases gradually as r_{eff} decreases. Observations during the very high state are plotted as filled circles and observations during the high/soft state are plotted as open squares. Figure 7b shows a surprising correlation between the power-law flux and r_{eff} . From Figure 7b it is apparent that the power-law flux is strongly correlated with r_{eff} and increases steeply for $r_{eff} \lesssim 5.5$, indicating that the physical mechanism responsible for producing the power-law emission is linked to the inner disk region. The correlation between r_{eff} and the power-law flux implies that the relativistic electrons are produced very near the inner accretion disk. Moreover, it is reasonable that the hard X-ray spectrum will also be produced in the inner disk region since there is a copious supply of soft seed photons there.

Figures 8a & b show r_{eff} and α vs. the luminosity in Eddington units, where

$L_{Edd} = 8.78 \times 10^{38}$ erg s $^{-1}$ for $m = 7.02$. Figure 8a indicates that r_{eff} decreases dramatically when the luminosity exceeds $l \sim 0.17$ and Figure 8b shows that the photon index does not vary systematically with luminosity. Both of these results are unexpected for canonical outburst states, for which the parameters vary smoothly (e.g. Ebisawa et al. 1994).

5. Spin of the Black Hole

Zhang et al. (1997a) outline general relativistic corrections that must be made to the inner disk radius derived from the multicolor disk model to determine the true inner disk radius. A formula for the gravitational energy release per unit area from the surface of a geometrically thin, optically thick accretion disk, corrected for general relativistic effects including black hole spin, is given by Page & Thorne (1974) and Zhang et al. (1997a). This formula assumes that the disk extends all the way down to the last stable orbit. The effective temperature of the disk peaks at a radius

$$r_{peak} = r_{last}/\eta, \quad (5)$$

where r_{last} is the last stable orbit and η is a function of the black hole angular momentum. There is a general relativistic correction to the spectral hardening factor, $f_{GR}(\theta, a_*)$, and an additional change of the observed flux due to viewing angle, $g(\theta, a_*)$ (Zhang et al. 1997a). In the Newtonian limit, $g(\theta, a_*) = \cos \theta$. Zhang et al. (1997a) find that these GR effects cause the spectrum to be redshifted at small θ and blueshifted at large θ . Also, gravitational focussing causes the flux to be smaller than the Newtonian flux at small θ and greater at large θ . Fortunately, the inclination angle and high angular momentum of GRO J1655–40 conspire to make these general relativistic corrections less than one-tenth the $\pm 24\%$ uncertainty in the inner disk radius due to the conventional spectral hardening factor, $f = 1.7 \pm 0.2$ (see Eq. (4)) (determined from data in Zhang et al. (1997a)). The important result of Zhang et al.’s analysis is that r_{eff} is the radius of the peak emission

region r_{peak} and not the inner disk radius.

The formula for the last stable prograde orbit (r_{last}) around a Kerr black hole from Bardeen, Press & Teukolsky (1972) is:

$$r_{last} = \left[3 + A_2 - [(3 - A_1)(3 + A_1 + 2A_2)]^{1/2} \right]; \quad (6)$$

$$A_1 = 1 + (1 - a_*^2)^{1/3} \left[(1 + a_*)^{1/3} + (1 - a_*)^{1/3} \right]; \quad (7)$$

$$A_2 = (3a_*^2 + A_1^2)^{1/2}, \quad (8)$$

where $a_* = a/r_g$ is the specific angular momentum, $a = J/Mc$, J is the black hole angular momentum, and $r_g = GM/c^2$. The last stable orbit around a maximally rotating prograde black hole ($a_* = +1$) can extend almost to the event horizon, GM/c^2 , whereas in the nonrotating Schwarzschild case, the last stable orbit is at $6 GM/c^2$.

The solutions for r_{peak} , r_{last} , η , and a_* are listed in Table 3. It is important to note that equation (5) assumes the disk extends all the way down to the last stable orbit, and therefore cannot be valid throughout most of the observations presented here. However, assuming the lowest observed value of r_{eff} (1.64) corresponds to the disk extending all the way down to the last stable orbit, we can use Table 3 to estimate the angular momentum of the spinning black hole in GRO J1655–40 and find $a_* \sim 0.997$ with $r_{last} \sim 1.3$.

The dominant source of uncertainty in this calculation is due to the spectral hardening factor ($f = 1.7 \pm 0.2$), which yields an uncertainty of 24% in the value of r_{eff} (see Eq. (4)). Taking this uncertainty into account, and since r_{eff} scales linearly with the assumed distance (see Eq. (1)), applying the firm distance upper limit of 5 kpc from Tingay et al. (1995), we obtain $r_{eff}(min) < 3.2$, which corresponds to $a_* > 0.9$ and $r_{last} \lesssim 2.2$. Therefore, it appears likely that GRO J1655–40 contains a rapidly rotating black hole with $a_* > 0.9$, in agreement with the results of Zhang et al. (1997a) who find $a_* = 0.93$.

6. The Flaring Episodes & the Comparison to GRS 1915+105

GRS 1915+105 and GRO J1655–40 are among the few Galactic sources known to produce superluminal radio jets (Mirabel & Rodriguez 1994, 1998; Tingay et al. 1995; Hjellming & Rupen 1995). Although no dynamical mass estimate for the compact primary in GRS 1915+105 exists, both sources are suspected of containing rapidly rotating black holes. Furthermore, GRS 1915+105 and GRO J1655–40 have exhibited similar, large changes in the temperatures and radii of their inner accretion disks coupled with power-law flares. During the GRS 1915+105 flares, T_{col} increased by a factor of two from 1 keV to 2.2 keV and r_{col} decreased by a factor of four from ~ 80 km to 20 km (Belloni et al. 1997b). The photon index increased from 2.2 to 3.6 and the power-law flux increased by a factor of six in the 2–50 keV band (Belloni et al. 1997a). Similarly for GRO J1655-40, during the flares T_{col} increased from 1.3 to 1.9 keV and r_{col} decreased by a factor of ~ 3.5 , while the photon index increased from 2.2 to 2.7 and the power-law flux increased by a factor of seven in the 2–50 keV band.

Belloni et al. (1997a,b) explain the flaring behavior of GRS 1915+105 by the removal and replenishment of the matter forming the inner part of an optically thick disk, probably caused by a Lightman-Eardley type thermal-viscous instability (Lightman & Eardley 1974) analogous to the limit cycle instability in dwarf novae. In this picture, the accretion disk has a central hole with radius R_{max} . The disk is slowly refilled on the viscous time scale at R_{max} from the outside by material whose radiation is too soft to be detected in the 2–20 keV band. When the inner disk reaches some critical radius, the disk suddenly ‘switches on’ and a flare occurs as a heating wave propagates outward through the central disk from the inner radius. The hot radiating material falls into the central black hole, emptying the inner disk. The cycle then starts over again.

The thermal instability model of Belloni et al. (1997a,b) describes the behavior of

GRS 1915+105 well, but it cannot account for the variability time scale of GRO J1655–40. The flares in GRS 1915+105 are observed on a time scale of ~ 100 seconds, whereas the flares in GRO J1655–40 occur on a time scale of a few days. In the Belloni et al. model, flares are expected to repeat on the time scale necessary to refill the inner disk, which is approximately the viscous time scale at the larger inner disk radius, R_{max} . Belloni et al. (1997b) express the viscous time scale (in our units) as:

$$t_{visc} = 6 \times 10^{-8} \alpha_v^{-1} m \dot{m}^{-2} r^{7/2} \text{ s}, \quad (9)$$

where α_v is the Shakura-Sunyaev viscosity parameter. We can estimate the mass accretion rate for GRO J1655–40 from Fig. 8a assuming $\dot{m} = l$. For $\alpha_v = 0.1$, $m = 7.02$, $\dot{m} = 0.15$, and $r = 5$, equation (9) implies $t_{visc} = 0.05$ seconds for GRO J1655–40, which is some six orders of magnitude shorter than the observed ~ 1 -day flaring time scale. Therefore, the thermal instability model of Belloni et al. cannot be responsible for the flaring behavior observed in GRO J1655–40. Instead, the time scale of the flaring behavior in GRO J1655–40 is comparable to the viscous time scale of the *outer* disk, where $t_{visc} \sim 1$ -day for $r \sim 300$. This flaring time scale is close to the 6-day X-ray delay (relative to the optical) that occurred during the 1996 April outburst of GRO J1655–40, which Hameury et al. (1997) identified with the viscous time scale needed to rebuild the inner disk. Changes in the behavior of an accreting system on this time scale can be associated with changes in the mass accretion rate. The following section explores the possibility that the changes in the inner disk radius during the flares of GRO J1655–40 are due to the effects of radiation drag in the inner disk and changes in the mass accretion rate.

7. Flaring Behavior and the Transition to Rapid Radial Inflow

7.1. Radiation Drag Force on the Inner Disk

In general relativity, when accreting material reaches the last stable orbit, the flow makes a transition from a Keplerian disk with slow inward drift to rapid radial infall. The azimuthal drag force caused by radiation drag force in the inner accretion disk can cause a transition to radial inflow at radii larger than the last stable orbit by removing enough angular momentum to overcome the centrifugal barrier (Miller, Lamb, & Psaltis 1998). Radiation drag can remove up to $\sim 20\%$ of the specific angular momentum of the accreting material (Miller & Lamb 1996). Since the angular momentum of the accreting material in the inner disk is not much higher than the angular momentum at the last stable orbit, radiation drag can result in large changes of the inner disk radius. The angular momentum per unit mass of an orbiting test particle around a prograde Kerr black hole in geometrized units is given by (Bardeen, Press & Teukolsky 1972):

$$L = \frac{(r^2 - 2a_*r^{1/2} + a_*^2)}{(r^3 - 3r^2 + 2a_*r^{3/2})^{1/2}}, \quad (10)$$

where r is in units of $r_g = GM/c^2$. Table 4 lists the radius of the last stable orbit for a few values of a_* and the radius (r_{infall}) at which the accretion flow makes the transition to radial infall if the maximum of 20% of the angular momentum is removed from the accreting material by radiation drag. For example, for $a_* = 0.9$, the removal of 20% of the specific angular momentum from the accretion flow causes the transition to radial infall at $r = 5.1$ instead of at the last stable orbit ($r = 2.3$). This is similar to the changes in r_{eff} from ~ 5.5 to 1.6 observed in GRO J1655–40 during the flares.

As discussed in the previous section, the ~ 1 -day time scale of the flaring behavior in GRO J1655–40 is comparable to the viscous time scale of the *outer* disk, which is associated with changes in the mass accretion rate. An increase in the mass accretion rate results in a corresponding increase in the optical depth in the disk. As the optical depth increases, the radiation from the inner disk cannot penetrate as far into the disk before it

is scattered, lessening the effects of radiation drag in the inner disk. As a result, we expect the inner accretion disk to approach the last stable orbit when the mass accretion rate, and correspondingly the optical depth, are high. When the mass accretion rate and optical depth are lower, we expect the transition from a Keplerian flow to radial inflow to occur at a larger radius (Miller, Lamb, & Psaltis 1998). Precisely this behavior is exhibited by GRO J1655–40 in Figure 8a: r_{eff} decreases when the luminosity (and therefore the mass accretion rate) exceeds a critical value ($l \sim 0.17$) during the flares, and r_{eff} increases for lower luminosities and accretion rates. We find that both the variability time scale and behavior of the inner disk radius during the flaring episodes in GRO J1655–40 are consistent with the radiation drag model described above, but detailed simulations will be required to prove this hypothesis.

7.2. Bulk-Motion Comptonization

It is possible that the power-law component during the very high and high/soft states is produced via bulk-motion Comptonization (BMC). BMC models (Ebisawa, Titarchuk & Chakrabarti 1996; Titarchuk, Mastichiadis & Kylafis 1997) propose that in the high/soft state the power-law component is produced by the Comptonization of soft photons due to the bulk motion of an almost freely-falling, Thomson optically-thick, convergent accretion flow near the black hole, instead of by the thermal motion of electrons in a corona. In the high/soft state, the Comptonizing medium is cooled by inverse Compton scattering off the copious soft photons from the Keplerian disk. The cooler converging inflow then rushes towards the black hole, producing a relatively steep power-law with $\alpha \sim 2.5$. In the low/hard state, there are few soft photons to cool the Comptonizing medium and the spectrum consists primarily of a hard power-law component ($\alpha \sim 1.5$) due to up-scattering of soft disk photons by hot thermal electrons in a corona. Detailed simulations of bulk-motion

Comptonization around a Kerr black hole will be necessary to test the relevance of the model in the case of GRO J1655–40. In any event, the presence of a Compton reflection component during the flares (§3.1) may be a complication for BMC models because the bulk flow in which the Comptonization occurs is (Thomson) optically thick, which would be expected to trap the reflected component in the advecting flow so that it could not escape to the observer (Grove et al. 1998).

8. Comparison to Nova Muscae 1991 & the ADAF Model

Nova Muscae 1991 (GRS 1124–68) was discovered on 1991 January 8 (Makino et al. 1991; Lund & Brandt 1991). The optical counterpart was subsequently identified and observations show that the source is a low mass X-ray binary containing a black hole primary with $M = 5.0\text{--}7.5 M_{\odot}$ (Orosz et al. 1996). Detailed observations of the source in outburst were made by Ebisawa et al. (1994) using the Ginga satellite commencing on 1991 January 10 and extending for 239 days until the source was no longer detectable. We have plotted Ebisawa et al.’s spectral parameters for Nova Muscae 1991 in Figures 9a–d. The corrections for spectral hardening (Eqs. (3) & (4)) have been applied to the Nova Muscae data. Figure 9 should be compared to Figure 3 for GRO J1655–40. It is apparent from Figure 9 that Nova Muscae 1991 does not display the hard flaring behavior observed in GRO J1655–40. During the first 40 days after outburst Nova Muscae 1991 is in the very high state and then enters the high/soft state. The open squares in Figure 9c from days 60 to 100 represent a fixed power-law photon index of 2.6. During this time, Ebisawa et al. state that the hard X-ray flux above 7 keV was so weak that the photon index could not be accurately determined. Over the next ~ 70 days following this period, the source underwent a soft-to-hard transition during which α decreased from 2.2 to 1.5 and T_{eff} fell from 0.35 keV to 0.15 keV.

Figures 10a & b show T_{eff} and the 2–100 keV power-law flux vs. r_{eff} for Nova Muscae 1991 for comparison to Figures 7a & b for GRO J1655–40. Comparing Figures 7b & 10b, it is apparent that both Nova Muscae 1991 and GRO J1655–40 exhibit the same behavior: the power-law flux increases as r_{eff} decreases. The dramatic increase in the power-law flux with decreasing radius indicates that the physical mechanism responsible for producing the power-law emission is linked to the inner disk region (within $14r_g$ for Nova Muscae 1991 (see Fig. 10 caption)).

The Advection Dominated Accretion Flow (ADAF) model (Narayan & Yi 1994) has been used successfully to describe the soft-to-hard transition observed in Nova Muscae 1991 (Esin et al. 1997a) and Cyg X-1 (Esin et al. 1997b). Figure 6 shows the 2–12 keV and 20–100 keV luminosity in Eddington units for GRO J1655–40, for comparison to Figure 12a in Esin et al. (1997a) for Nova Muscae 1991. Esin et al. (1997a) predicted that the photon index should have risen sharply to ~ 4 or 5 in the high/soft state prior to the soft-to-hard transition (see their Fig. 12d), during the time when Ebisawa et al. were unable to fit the power-law component and therefore fixed the photon index (Fig. 9c). Similarly, this prediction of the ADAF model may explain the peculiar spectral behavior of GRO J1655–40 during those observations where the apparent power-law component was steep and poorly-determined (see Table 1, note entries marked by the footnote g).

Notice from Figure 9b that the soft-to-hard transition in Nova Muscae 1991 is accompanied by an apparent decrease in the inner disk radius after day 150. We observed the same behavior in GRO J1655–40 (Fig. 3b) after day 465. Ebisawa et al. (1994) note that electron scattering affects the inner disk spectrum through Comptonization of the emergent spectrum (Shakura & Sunyaev 1973). As discussed in § 3, such a Comptonized spectrum may be approximated by a diluted blackbody where the spectral shape is the same as a blackbody with temperature $T_{col} = fT_{eff}$ and the observed inner disk radius is smaller

than the actual peak emission radius by $r_{col} = r_{eff}/f^2$. However, at low accretion rates ($\dot{m} \leq 0.1$), this approximation breaks down (Shimura & Takahara 1995). The apparent decrease in r_{eff} after day 465 in GRO J1655–40 just prior to turnoff can be explained by an increase in the spectral hardening factor rather than a decrease in the inner disk radius.

9. QPOs

Recently, high frequency QPOs have been observed with RXTE from GRS 1915+105 and GRO J1655–40. It has been proposed that these QPOs are produced by X-ray modulation at the precession frequency of an accretion disk experiencing frame dragging caused by a rotating black hole (Cui et al. 1998). According to this model, the 300 Hz QPO present during certain spectral states in GRO J1655–40 (Remillard et al. 1997, 1998), implies a specific angular momentum for the black hole $a_* = +0.95$ (Cui et al. 1998) with $r_{last} = 1.94$.

Figure 3b shows the times QPOs are present during our observations (Remillard et al. 1998). The presence of the 300 Hz QPO is indicated by an open triangle and the presence of the variable frequency QPOs (< 28 Hz) is indicated by an open square at the top of the figure. From Figure 3b it is clear that the 300 Hz QPO is present over a range of inner disk radii ($r_{eff} = 1.6\text{--}5.0$), and therefore it cannot be due to the precession frequency of the inner disk at the last stable orbit. The presence of the 300 Hz QPO for $r_{eff} = 1.6\text{--}5.0$ instead appears to favor models that can produce a constant QPO frequency over a range of inner disk radii, such as the ‘diskoseismic’ models in which the QPO is due to radial g-mode oscillations in the inner accretion disk (Nowak & Wagoner 1992, 1993; Perez et al. 1997). However, the diskoseismic models have trouble reproducing the observed energy dependence of high-frequency QPOs for the case of GRS 1915+105 (Morgan, Remillard, & Greiner 1997).

Figures 11a & b illustrate a surprising correlation between QPO frequency, r_{eff} , and the 2–100 keV power-law flux for the variable frequency (14–28 Hz) QPOs. Figure 11a shows that the QPO frequency decreases as r_{eff} decreases, which is contrary to the behavior expected if the QPO were tied to the Keplerian frequency at the shrinking inner edge of the disk. The mechanism producing these QPOs is unclear.

10. Conclusions

We have analyzed RXTE data obtained for GRO J1655–40 covering a complete, 16-month outburst cycle of the source. These data comprise a nearly continuous observation of the source with the ASM, and 52 pointed observations with the PCA and HEXTE instruments. Satisfactory fits to nearly all the PCA/HEXTE data were obtained with a multicolor disk plus power-law model (with allowance for some minor modifications). The source exhibits two principal outburst states which we associate with the very high and high/soft states. During the very high state, the spectrum was often dominated by a power-law component with $\alpha = 2.3\text{--}2.7$. The source exhibited intense flares which were correlated with changes (hours to days) in both the temperature and radius of the inner accretion disk. During the high/soft state, the spectrum was dominated by the soft thermal emission from the accretion disk with approximately constant inner disk radius and temperature. The power-law component was relatively weak with $\alpha \sim 2\text{--}3$. During the last few observations, the source underwent a transition to the low/hard state.

An important discovery of this work is the *variability of the inner radius of the accretion disk*, from $r_{eff} = 1.6$ to ~ 5.5 on a time scale of a few days. GRS 1915+105 also exhibited power-law flares associated with changes in the temperature and radius of the inner accretion disk. These events may be explained by the removal and replenishment of the inner accretion disk, probably caused by a thermal-viscous instability analogous to the

limit cycle instability in dwarf novae (Belloni et al. 1997a,b). However, the time scale of the flares in GRO J1655–40 is some six orders of magnitude longer than predicted by the Belloni et al. model for GRS 1915+105. We find that both the variability time scale and behavior of the inner disk radius during the flaring behavior in GRO J1655–40 are consistent with the effects of radiation drag in the inner disk and changes in the mass accretion rate.

The principle discovery of this work is a *strong correlation between the flux in the power-law component and the radius of the inner accretion disk* (Fig. 7b). This correlation implies that the relativistic electrons are produced very near the inner accretion disk. Moreover, it is reasonable that the hard X-ray spectrum will also be produced in the inner disk region since there is a copious supply of soft seed photons there. The same correlation between the inner disk radius and power-law flux is also evident in the spectral results for Nova Muscae 1991 presented by Ebisawa et al. (1994) and illustrated here (Fig. 10b). This correlation argues against the two-phase accretion models, which consist of a ‘cold’ disk sandwiched between two plane-parallel slabs of corona consisting of thermal electrons (e.g. Haardt & Maraschi 1991, 1993), and in favor of an inner disk-fed corona. The same conclusion was reached by Dove et al. (1997, 1998) who found that plane-parallel corona models do not fit the observed spectra of Cyg X-1. Instead, they found that the spectra are best described by a hot spherical corona surrounded by an exterior cold disk.

Using the results of Remillard et al. (1998), we find the steady 300 Hz QPO is present over a range in inner disk radii (1.6–5.0 r_g), and therefore cannot be due to the precession frequency of the inner disk at the last stable orbit (Cui et al. 1998). However, we do confirm that GRO J1655–40 contains a rapidly rotating black hole with $a_* > 0.9$, based on the inferred value of the last stable orbit (Zhang et al. 1997a). We also find that the 14–28 Hz QPO frequency decreases as r_{eff} decreases (Fig. 11a), which is the opposite behavior expected if the QPO frequency were associated with matter moving inward through a

Keplerian disk. The mechanism producing these QPOs is still unclear.

Partial support for J.M. and G.S. was provided by the Smithsonian Institution Scholarly Studies Program. R.R. was supported, in part, by NASA grant NAG5-3680. C.B. acknowledges support from NSF grant AST 9730774. The authors wish to thank D. Psaltis and A. Esin for helpful discussions. This research has made use of data obtained through the High Energy Astrophysics Science Archive Research Center Online Service, provided by the NASA/Goddard Space Flight Center.

REFERENCES

Bailyn, C. D., et al. 1995, *Nature*, 374, 701

Bardeen, J. M., Press, W. H. & Teukolsky, S. A. 1972, *ApJ*, 178, 347

Belloni, T., Mendez, M., van der Klis, M., Hasinger, G., Lewin, W. H. G., & van Paradijs, J. 1996, *ApJ*, 472, L107

Belloni, T., Mendez, M., King, A. R., van der Klis, M., & van Paradijs, J. 1997a, *ApJ*, 479, L145

Belloni, T., Mendez, M., King, A. R., van der Klis, M., & van Paradijs, J. 1997b, *ApJ*, 488, L109

Cui, W., Zhang, S. N. & Chen, W. 1998, *ApJ*, 492, 53.

Done, C., Mulchaey, J. S., Mushotzky, R. F., & Arnaud, K. A. 1992, *ApJ*, 395, 275

Dove, J. B., Wilms, J., Maisack, M., & Begelman, M. C., 1997, *ApJ*, 487, 759

Dove, J. B., Wilms, J., Nowak, M. A., Vaughan, B. A., & Begelman, M. C., 1998, Submitted to MNRAS, astro-ph/9707322

Ebisawa, K. et al. 1994, *PASJ*, 46, 375

Ebisawa, K., Titarchuk, L. & Chakrabarti, S. K. 1996, *PASJ*, 48, 59

Esin, A. A., McClintock, J. E., & Narayan, R. 1997a, *ApJ*, 489, 865

Esin, A. A., Narayan, R., Cui, W., Grove, J. E., & Zhang, S. N. 1997b, astro-ph/9711167, Submitted to *ApJ*

Frank, J., King, A. & Raine, D. 1992, *Accretion Power in Astrophysics*, Cambridge University Press, Cambdrige, p. 78

Grove, J. E., Grindlay, J. E., Harmon, B. A., Hua, X.-M., Kazanas, D., & McConnell, M. 1998, astro-ph/9804268

Haardt, F. & Maraschi, L. 1991, *ApJ*, 380, L51

Haardt, F. & Maraschi, L. 1993, *ApJ*, 413, 507

Hameury, J.-M., Lasota, J.-P., McClintock, J. E. & Narayan, R. 1997, 489, 234

Hjellming, R. M. & Rupen, M. P. 1995, *Nature*, 375, 464

Inoue, H. 1991, in *Frontiers of X-ray Astronomy*, ed. Y. Tanaka & K. Koyama (Tokyo: Universal Academy Press), 291

Kalogera, V. & Baym, G. 1996, *ApJ*, 470, L61

Levine, A. M., Bradt, H., Cui, W., Jernigan, J. G., Morgan, E. H., Remillard, R., Shirey, R. E., & Smith, D. A. 1996, *ApJ*, 469, 33

Lightman, A. P. & Eardley, D. M. 1974, *ApJ*, 187, L1

Lund, N. & Brandt, S. 1991, *IAU Circ.* 5161

Magdziarz, P. & Zdziarski, A. A. 1995, *MNRAS*, 273, 837

Makino, F. & Ginga team 1991, *IAU Circ.* 5161

Makishima, K. et al. 1986, *ApJ*, 308, 635

McClintock, J. E. 1998, in *Accretion Processes in Astrophysical Systems*, ed. S. S. Holt & T. Kallman (Woodbury, NY: AIP), 290

Mendez, M. & van der Klis, M. 1997, *ApJ*, 479, 926

Miller, M. C. & Lamb, F. K. 1996, *ApJ*, 470, 1033

Miller, M. C., Lamb, F. K., & Psaltis, D. 1998, Accepted to *ApJ*

Mioduszewski, A. J., Hjellming, R. M., Rupen, M. P., McCollough, M., Waltman, E. B., & Poolet, G. G. 1997, *BAAS*, 29, 1387

Mirabel, I. F. & Rodriguez, L. F. 1994, *Nature*, 371, 46

Mirabel, I. F. & Rodriguez, L. F. 1998, *Nature*, 392, 673

Mitsuda, K. et al. 1984, PASJ, 36, 741

Morgan, E. H., Remillard, R. A., & Greiner, J. 1997, ApJ, 482, 993

Morrison, R. & McCammon, D. 1983, ApJ, 270, 119

Narayan, R. & Yi, I. 1994, ApJ, 428, 13

Narayan, R., Barret, D., & McClintock, J. E. 1997, ApJ, 482, 448

Newell, S. J., Garrett, M. A., & Spencer, R. E. 1998, MNRAS, 293, L17

Nowak, M. A. 1995, PASP, 107, 1207

Nowak, M. A. & Wagoner, R. V. 1992, ApJ, 393, 697

Nowak, M. A. & Wagoner, R. V. 1993, ApJ, 418, 187

Nowak, M. A., Wagoner, R. V., Begelman, M. C., & Lehr, D. E. 1997, ApJ, 477, L91

Orosz, J. A., Bailyn, C. D., McClintock, J. E., & Remillard, R. A. 1996, ApJ, 468, 380

Orosz, J. A., Remillard, R. A., Bailyn, C. D., & McClintock, J. E. 1997, ApJ, 478, L83

Orosz, J. A. & Bailyn, C. D. 1997, ApJ, 477, 876

Page, D. N. & Thorne, K. S. 1974, ApJ, 191, 499

Perez, C. A., Silbergbeit, A. S., Wagoner, R. V., & Lehr, D. E. 1997, ApJ, 476, 589

Remillard, R. A., Morgan, E. H., McClintock, J. E., Bailyn, C. D., Orosz, J. A., & Greiner, J., 1997, to appear in *Annals of the N. Y. Academy of Sciences*, presented at the 18th Texas Symposium

Remillard, R. A., Morgan, E. H., McClintock, J. E., Bailyn, C. D., & Orosz, J. A. 1998, ApJ, in press

Shakura, N. I. & Sunyaev, R. A. 1973, A&A, 24, 337

Shimura, T. & Takahara, F. 1995, ApJ, 445, 780

Shrader, C. & Titarchuk, L. 1998, *ApJ*, 499, L31

Smith, D. M., Heindl, W. A., Swank, J., Leventhal, M., Mirabel, I. F. & Rodriguez, L. F. 1997, *ApJ*, 489, L51

Tanaka, Y. & Lewin, W. H. G. 1995, in *X-ray Binaries*, ed. W. H. G. Lewin, J. van Paradijs, & E. P. J. van den Heuvel (Cambridge: Cambridge Univ. Press)

Tanaka, Y. & Shibasaki, N. 1996, *ARA&A*, 34, 607

Tingay, S. J. et al. 1995, *Nature*, 374, 141

Titarchuk, L., Mastichiadis, A., & Kylafis, N. D. 1997, *ApJ*, 487, 834

van der Hooft, F., Heemskerk, M. H. M., Alberts, F., & van Paradijs, J. 1998, *A&A*, 329, 538

Zhang, S. N., et al. 1994, *IAU Circ.* 6046

Zhang, S. N. et al. 1996, *IAU Circ.* 6462

Zhang, S. N., Cui, W., & Chen, W. 1997a, *ApJ*, 482, L155

Zhang, S. N., Ebisawa, K., Sunyaev, R., et al. 1997b, *ApJ*, 479, 381

Fig. 1.— (a) The 2–12 keV ASM lightcurve (counts s^{−1}) and (b) the ratio of the ASM count rates (5–12 keV)/(3–5 keV) for GRO J1655–40. The labels in the top panel and the dashed vertical lines indicate different outburst states (see text). The small, solid vertical lines in the top panel indicate the times of pointed RXTE observations. The individual ASM dwells are plotted in (a) and the ratios of the one-day averages are plotted in (b).

Fig. 2.— Representative spectra from each of the observed spectral states of GRO J1655–40, along with the best fit model for (a, b) the very high state, (c, d) the high/soft state, and (e) the low/hard state. The individual components of the model are also shown. The 6-digit number in the upper left hand corner of each panel identifies the date of the observation (see Table 1). See the text for details on the spectral models and fitting. Although error bars are plotted for all the data, they are only large enough to be visible at the highest energies.

Fig. 3.— Spectral parameters for PCA/HEXTE observations of GRO J1655–40. The spectra were fit to a model of interstellar absorption plus multicolor disk plus power-law. The hydrogen column density was fixed at 0.89×10^{22} cm^{−2} (Zhang et al. 1997b). The quantities plotted here are (a) the effective temperature of the accretion disk (T_{eff}) in keV, (b) the inner disk radius r_{eff} in units of $r_g = GM/c^2$ for $M = 7.02M_\odot$, $\theta = 69^\circ 5$ (Orosz & Bailyn 1997), and $D = 3.2$ kpc (Hjellming & Rupen 1995) (see Eq. (1)), (c) the power-law photon index α , and (d) the power-law normalization K in units of photons s^{−1} cm^{−2} keV^{−1} at 1 keV. The presence of the 300 Hz QPO is indicated by an open triangle and the presence of the variable frequency QPOs (< 28 Hz) is indicated by an open square at the top of (b) (Remillard et al. 1998). Here and in several subsequent figures for which error bars are not visible, it is because they are comparable to or smaller than the plotting symbol.

Fig. 4.— Effect of the Fe absorption edge on the ratio data/model for a representative high/soft state spectrum (970320). Figure (a) shows the residuals for the interstellar absorption plus multicolor disk plus power-law only. Figures (b) & (c) show the effects

of a smeared Fe absorption edge applied to the power-law component (Ebisawa et al. 1994) at edge energies of 7.1 and 8.0 keV, respectively. The width of the absorption feature was kept fixed at 7 keV and the Fe optical depth was allowed to float.

Fig. 5.— Plot of (a) the total unabsorbed flux of GRO J1655–40, (b) the bolometric flux from the disk blackbody calculated using the formula: $Flux = 2\sigma ((R_{col}^2/D^2) \cos \theta) T_{col}^4$, and (c) the 2–100 keV flux from the power-law component. The units are 10^{-8} ergs s^{-1} cm^{-2} . The ratio of the disk blackbody to the total unabsorbed flux is shown in (d). The total and power-law fluxes for the ten poorly-fit high/soft state spectra have been omitted because of uncertainty in the nature of the quasi-power-law component. Reducing the lower energy bound from 2 keV to 1 keV increases the power-law fluxes by $\sim 50\%$.

Fig. 6.— Log plot of the 2–12 keV luminosity (filled circles) and the 20–100 keV luminosity (open squares) in Eddington units for GRO J1655–40. The data points for the ten poorly-fit high/soft state spectra have been omitted because of uncertainty in the nature of the quasi-power-law component.

Fig. 7.— Plot of (a) T_{eff} vs. r_{eff} and (b) 2–100 keV power-law flux vs. r_{eff} . Observations during the very high state are plotted as filled circles and observations during the high/soft state are plotted as open squares. The last three observations on days 476, 480, and 487 have been omitted because the multicolor disk model no longer yields reasonable physical values for the inner disk radius. The data points for the ten poorly-fit high/soft state spectra have been omitted because of uncertainty in the nature of the quasi-power-law component.

Fig. 8.— Plot of (a) r_{eff} vs. l and (b) α vs. l , where l is the bolometric disk luminosity plus the 2–100 keV power-law luminosity in Eddington units ($L_{Edd} = 8.8 \times 10^{38}$ erg s^{-1} for $M = 7.02M_{\odot}$). Data during the very high state are plotted as filled circles and data during the high/soft state are plotted as open squares. The last three data points on days 476,

480, and 487 have been omitted from (a) because the multicolor disk model no longer yields reasonable physical values for the inner disk radius. These three data points are plotted as open triangles in (b). The data points for the ten poorly-fit high/soft state spectra have been omitted from both (a) & (b) because of uncertainty in the nature of the quasi-power-law component.

Fig. 9.— Spectral parameters for Ginga observations of Nova Muscae 1991 (GRS 1124–68) from Ebisawa et al. (1994) for comparison to Figure 3 for GRO J1655–40. The four quantities plotted are (a) the effective temperature at the inner disk radius in keV, (b) the effective inner disk radius in kilometers, for $D = 1$ kpc, (c) the power-law photon index, and (d) the power-law normalization K in units of photons $\text{s}^{-1} \text{cm}^{-2} \text{keV}^{-1}$ at 1 keV as a function of days after outburst. r_{eff} is in units of $r_g = GM/c^2$ where $M = 6M_\odot$, $\theta = 60^\circ$ (Orosz et al. 1996), and $D = 2.5$ kpc (Ebisawa et al. 1994). Following Ebisawa et al. (1994) and for the purposes of this illustration we adopt $D = 2.5$ kpc. However, the actual distance is probably closer to twice this value (see § 4.1 in Esin et al. 1997), which would double the value of r_{eff} . The open squares in (c) correspond to a fixed value of the photon index: $\alpha = 2.6$.

Fig. 10.— Plot of (a) T_{eff} vs. r_{eff} and (b) 2–100 keV power-law flux vs. r_{eff} for Nova Muscae 1991. This figure should be compared to Figure 7 for GRO J1655–40. r_{eff} is in units of $r_g = GM/c^2$ where $M = 6M_\odot$, $\theta = 60^\circ$ (Orosz et al. 1996), and $D = 2.5$ kpc (Ebisawa et al. 1994). Following Ebisawa et al. (1994) and for the purposes of this illustration we adopt $D = 2.5$ kpc. However, the actual distance is probably closer to twice this value (see § 4.1 in Esin et al. 1997), which would double the value of r_{eff} .

Fig. 11.— Correlation between (a) QPO frequency and r_{eff} and (b) QPO frequency and the 2–100 keV power-law flux for 14–28 Hz QPOs. The 28.3 Hz QPO plotted with a triangle appears only in the sum of the high/soft state observations (days 255–465) (Remillard et al.

1998), and is plotted here at the average r_{eff} and power-law flux for the high/soft state.

Table 1. Spectral Parameters for GRO J1655–40^a

Date (yymmdd UT)	Day ^b (MJD 50198+)	T_{eff} (keV)	r_{eff} (r_g) ^c	Photon Index	Power-law Norm. (phot s^{-1} cm^{-2} keV $^{-1}$ at 1 keV)	τ_{Fe}^d	χ^2_{ν} (dof)	Energy (keV)
960509	14.8	0.73 ± 0.01^f	6.42 ± 0.04^f	$5.77_{-0.19}^{+0.21}g$	$4620_{-1900}^{+3640}g$	–	1.65(39) ^f	–
960510	15.5	0.72 ± 0.01^f	6.57 ± 0.04^f	$6.47_{-0.20}^{+0.33}g$	$31400_{-13100}^{+47100}g$	–	1.13(39) ^f	–
960511	16.5	0.73 ± 0.01^f	6.48 ± 0.04^f	$5.69_{-0.26}^{+0.30}g$	$3930_{-2030}^{+5210}g$	–	1.45(39) ^f	–
960512	17.4	0.73 ± 0.01^f	6.36 ± 0.05^f	$5.75_{-0.26}^{+0.32}g$	$4900_{-2530}^{+7140}g$	–	1.13(39) ^f	–
960725	91.4	0.77 ± 0.01	5.37 ± 0.04	2.28 ± 0.01	5.90 ± 0.18	–	1.57(248)	2.5-100
960801 ^h	98.4	1.13 ± 0.01	1.64 ± 0.06	2.68 ± 0.01	62.7 ± 1.3	–	1.35(246)	2.5-100
960806	103.7	0.93 ± 0.01	2.70 ± 0.05	2.67 ± 0.01	44.1 ± 0.9	–	0.84(248)	2.5-100
960815	112.6	0.76 ± 0.01	5.35 ± 0.04	2.30 ± 0.02	$5.90_{-0.35}^{+0.37}$	–	2.11(150)	2.5-50
960816	113.4	0.78 ± 0.01	4.49 ± 0.07	2.42 ± 0.01	18.9 ± 0.6	–	1.23(248)	2.5-100
960822	119.5	0.76 ± 0.01	4.96 ± 0.05	2.46 ± 0.01	16.4 ± 0.5	–	0.88(248)	2.5-100
960829 ^h	126.4	1.09 ± 0.01	$1.98_{-0.09}^{+0.07}$	2.78 ± 0.03	$65.5_{-2.2}^{+2.4}$	–	0.73(246)	2.5-50
960904	132.3	0.76 ± 0.01	5.34 ± 0.05	2.40 ± 0.02	$9.59_{-0.41}^{+0.43}$	–	1.89(150)	2.5-50
960909	138.0	0.78 ± 0.01	5.07 ± 0.05	2.37 ± 0.01	9.49 ± 0.22	–	1.50(248)	2.5-100
960920	148.2	0.75 ± 0.01	5.44 ± 0.04	2.23 ± 0.02	$4.31_{-0.22}^{+0.23}$	–	1.60(150)	2.5-50
960926	154.3	0.75 ± 0.01	5.72 ± 0.04	1.97 ± 0.03	$0.93_{-0.06}^{+0.07}$	–	1.32(150)	2.5-50
961003	161.6	0.75 ± 0.01	5.65 ± 0.04	2.14 ± 0.02	$2.16_{-0.12}^{+0.13}$	–	0.82(150)	2.5-50
961015	173.5	0.78 ± 0.01	5.39 ± 0.04	2.18 ± 0.01	3.83 ± 0.13	–	1.09(248)	2.5-100
961022	180.1	0.77 ± 0.01	5.55 ± 0.05	2.23 ± 0.01	4.86 ± 0.15	–	0.92(248)	2.5-100
961027	185.6	0.80 ± 0.01	4.56 ± 0.06	2.59 ± 0.02	26.0 ± 1.5	–	0.60(91)	2.5-20
961102A ^h	191.2	$0.84_{-0.02}^{+0.01}$	$2.15_{-0.09}^{+0.10}$	2.57 ± 0.01	35.9 ± 0.8	–	1.26(246)	2.5-100
961102B ^h	191.3	1.09 ± 0.01	$1.69_{-0.09}^{+0.07}$	2.64 ± 0.01	$53.4_{-1.5}^{+1.9}$	–	1.00(246)	2.5-100
970105	255.4	0.64 ± 0.01	$5.72_{-0.06}^{+0.07}$	1.94 ± 0.04	$0.92_{-0.12}^{+0.13}$	0.40 ± 0.25	1.08(149)	2.5-50
970112	262.1	0.62 ± 0.01	6.27 ± 0.07	2.00 ± 0.06	0.61 ± 0.13	0.97 ± 0.33	0.88(149)	2.5-50
970121	271.0	0.55 ± 0.01	6.50 ± 0.05	1.65 ± 0.09	0.03 ± 0.01	–	0.82(91)	2.5-20
970126	276.9	0.57 ± 0.01	6.65 ± 0.10	2.17 ± 0.10	$0.48_{-0.13}^{+0.16}$	$1.79_{-0.48}^{+0.42}$	0.56(90)	2.5-20
970226	307.9	0.65 ± 0.01	6.62 ± 0.05	3.01 ± 0.08	$4.50_{-0.92}^{+1.06}$	10.2 ± 0.4	2.53(107)	2.5-30
970305	314.8	0.66 ± 0.01	6.70 ± 0.06	2.96 ± 0.08	$4.89_{-1.00}^{+1.15}$	7.23 ± 0.32	2.20(90)	2.5-20
970310	319.7	0.66 ± 0.01	6.61 ± 0.05	2.75 ± 0.08	$3.46_{-0.76}^{+0.89}$	$5.64_{-0.31}^{+0.29}$	1.53(90)	2.5-20
970320	329.9	0.67 ± 0.01	6.63 ± 0.04	2.43 ± 0.07	$1.99_{-0.42}^{+0.50}$	$3.62_{-0.32}^{+0.30}$	1.04(147)	2.5-49
970324	333.8	0.67 ± 0.01^f	6.61 ± 0.03^f	$2.70_{-0.35}^{+0.40}g$	$0.61_{-0.61}^{+1.26}g$	–	2.58(39) ^f	–
970404	344.7	0.67 ± 0.01	6.64 ± 0.04	2.41 ± 0.09	$1.88_{-0.45}^{+0.54}$	$3.76_{-0.35}^{+0.32}$	1.17(149)	2.5-50
970410	350.5	0.67 ± 0.01	6.58 ± 0.04	2.44 ± 0.09	$2.38_{-0.60}^{+0.71}$	$3.53_{-0.33}^{+0.30}$	0.86(90)	2.5-20
970416	356.8	0.66 ± 0.01	6.65 ± 0.05	2.96 ± 0.08	$4.19_{-0.91}^{+1.10}$	$9.03_{-0.39}^{+0.38}$	2.29(89)	2.5-20
970424	364.8	0.67 ± 0.01^f	6.58 ± 0.03^f	2.96 ± 0.65^g	$1.14_{-1.14}^{+6.05}g$	–	1.92(39) ^f	–
970430	370.6	0.68 ± 0.01^f	6.50 ± 0.03^f	3.50 ± 0.56^g	$4.76_{-4.76}^{+18.5}g$	–	2.33(39) ^f	–

Table 1—Continued

Date (yymmdd UT)	Day ^b (MJD 50198+)	T_{eff} (keV)	r_{eff} (r_g) ^c	Photon Index	Power-law Norm. (phot s ⁻¹ cm ⁻² keV ⁻¹ at 1 keV)	τ_{Fe}^d	$\chi^2_{\nu}^e$ (dof)	Energy (keV)
970508	378.5	0.70 ± 0.01^f	6.40 ± 0.03^f	$2.87^{+0.42}_{-0.38}g$	$1.07^{+2.47}_{-1.07}g$	–	2.04(39) ^f	–
970512	382.7	0.70 ± 0.01^f	6.40 ± 0.03^f	$5.10^{+0.55}_{-0.62}g$	$387^{+1400}_{-318}g$	–	1.90(39) ^f	–
970520	390.4	0.71 ± 0.01	6.31 ± 0.06	$2.89^{+0.10}_{-0.12}$	$3.86^{+1.37}_{-1.18}$	$4.82^{+0.51}_{-0.57}$	1.43(90)	2.5-20
970528	398.4	0.71 ± 0.01	6.30 ± 0.05	2.52 ± 0.08	$3.08^{+0.80}_{-0.68}$	$2.92^{+0.33}_{-0.35}$	0.91(147)	2.5-49
970605	406.3	0.69 ± 0.01	6.38 ± 0.06	2.86 ± 0.09	$4.71^{+1.30}_{-1.16}$	$4.73^{+0.36}_{-0.20}$	1.10(108)	2.5-30
970609	410.5	0.68 ± 0.01	6.49 ± 0.07	2.89 ± 0.11	$4.24^{+1.47}_{-1.24}$	$6.59^{+0.47}_{-0.51}$	1.10(90)	2.5-20
970619	420.3	0.67 ± 0.01	6.56 ± 0.04	2.24 ± 0.11	$1.38^{+0.47}_{-0.40}$	$3.39^{+0.33}_{-0.40}$	0.80(90)	2.5-20
970626	427.8	0.65 ± 0.01^f	6.71 ± 0.03^f	$3.35^{+0.76}_{-0.73}g$	$3.13^{+23.3}_{-3.13}g$	–	0.95(39) ^f	–
970704	435.5	0.61 ± 0.01	6.95 ± 0.04	2.64 ± 0.09	$1.82^{+0.52}_{-0.44}$	$6.10^{+0.27}_{-0.30}$	1.51(90)	2.5-20
970708	439.6	0.62 ± 0.01	6.59 ± 0.06	2.10 ± 0.10	$0.71^{+0.23}_{-0.20}$	$2.10^{+0.38}_{-0.45}$	0.79(90)	2.5-20
970714	445.3	0.60 ± 0.01	7.11 ± 0.05	2.53 ± 0.11	$1.31^{+0.47}_{-0.38}$	$5.13^{+0.35}_{-0.39}$	0.87(90)	2.5-20
970724	455.6	0.57 ± 0.01	6.60 ± 0.08	2.16 ± 0.05	$0.67^{+0.12}_{-0.10}$	$1.94^{+0.23}_{-0.24}$	1.09(149)	2.5-50
970729	460.4	0.51 ± 0.01	6.89 ± 0.12	2.22 ± 0.05	$0.94^{+0.13}_{-0.12}$	2.32 ± 0.25	0.88(90)	2.5-20
970803	465.7	0.46 ± 0.01	7.31 ± 0.12	2.52 ± 0.06	$0.87^{+0.13}_{-0.12}$	2.19 ± 0.26	1.01(90)	2.5-20
970814	476.5	0.31 ± 0.02	$5.57^{+0.94}_{-0.77}$	2.00 ± 0.01	0.76 ± 0.02	0.85 ± 0.07	0.87(149)	2.5-50
970818	480.6	0.33 ± 0.04	$1.82^{+0.94}_{-0.54}$	1.71 ± 0.02	0.14 ± 0.01	0.34 ± 0.10	0.78(119)	2.5-50
970825	487.5	0.26 ± 0.03	$3.12^{+1.45}_{-0.87}$	1.89 ± 0.11	0.02 ± 0.01	$1.20^{+0.53}_{-0.52}$	0.51(74)	2.5-17

^aUsed fixed $N_H = 0.89 \times 10^{22}$ cm⁻² (Zhang et al. 1997).

^bMidpoint of observation.

^c $r_g = GM/c^2$ for $M = 7.02M_{\odot}$ and Eq. (1) with $\theta = 69^{\circ}5$ (Orosz & Bailyn 1997) and $D = 3.2$ kpc (Hjellming & Rupen 1995).

^dFixed edge at 8.0 keV and width of 7 keV using ‘smedge’ model in XSPEC.

^ePCA = 2.5 – 20 keV & HEXTE > 20 keV.

^fDetermined from 2.5-10 keV using only interstellar absorption and multicolor disk blackbody models.

^gDetermined from 15-20 keV with fixed multicolor disk parameters determined from 2.5-10 keV.

^hFitted including a Compton reflection component model (see §3.1 and Table 2).

Table 2. Fit Parameters for Compton Reflection^a

Date (yymmdd UT)	Day ^b (MJD 50198+)	$\Omega/2\pi$ ^c	ξ ^d
960801	98.4	$0.88^{+0.09}_{-0.08}$	442^{+499}_{-272}
960829	126.4	$1.30^{+0.27}_{-0.35}$	$84.5^{+642}_{-79.2}$
961102A	191.2	0.58 ± 0.07	$1.01^{+12.0}_{-0.97}$
961102B	191.3	$1.15^{+0.11}_{-0.10}$	$0.013^{+41.4}_{-0.013}$

^aThe Compton reflection component was calculated using the ‘pexriv’ model in XSPEC version 10. The Fe and elemental abundances were fixed at the solar value. The disk temperature was fixed at 10⁵ K (Done et al. 1992), the inclination angle was fixed at 69°5 (Orosz & Bailyn 1997). No exponential cutoff of the power-law was applied.

^bMidpoint of observation.

^cNormalization of reflection.

^dThe ionization parameter $\xi = L/nR^2$, where L is the integrated incident luminosity between 5 eV and 300 keV, n is the density of the material, and R is the distance of the material from the illuminating source (Done et al. 1992).

Table 3. Determining r_{last} & a_* from r_{peak}

r_{peak} (r_g) ^a	r_{last} (r_g) ^a	η	a_*
1.58	1.24	0.782	0.998
1.66	1.28	0.771	0.997
1.75	1.33	0.760	0.996
1.98	1.45	0.736	0.99
2.80	1.94	0.692	0.95
3.08	2.10	0.683	0.93
3.44	2.32	0.675	0.90
4.42	2.91	0.658	0.80
5.22	3.39	0.650	0.70
5.94	3.83	0.645	0.60
6.61	4.23	0.640	0.50
7.24	4.61	0.637	0.40
7.85	4.98	0.634	0.30
8.43	5.33	0.632	0.20
9.00	5.67	0.630	0.10
9.55	6.00	0.628	0.00

^a $r_g = GM/c^2$

Table 4. Transition to Radial Inflow

a_*	r_{last} (r_g) ^a	r_{infall} (r_g) ^a
0.0	6.0	15.0
0.5	4.2	10.3
0.85	2.6	6.0
0.90	2.3	5.1
0.99	1.5	2.7
0.998	1.2	2.1

^a $r_g = GM/c^2$

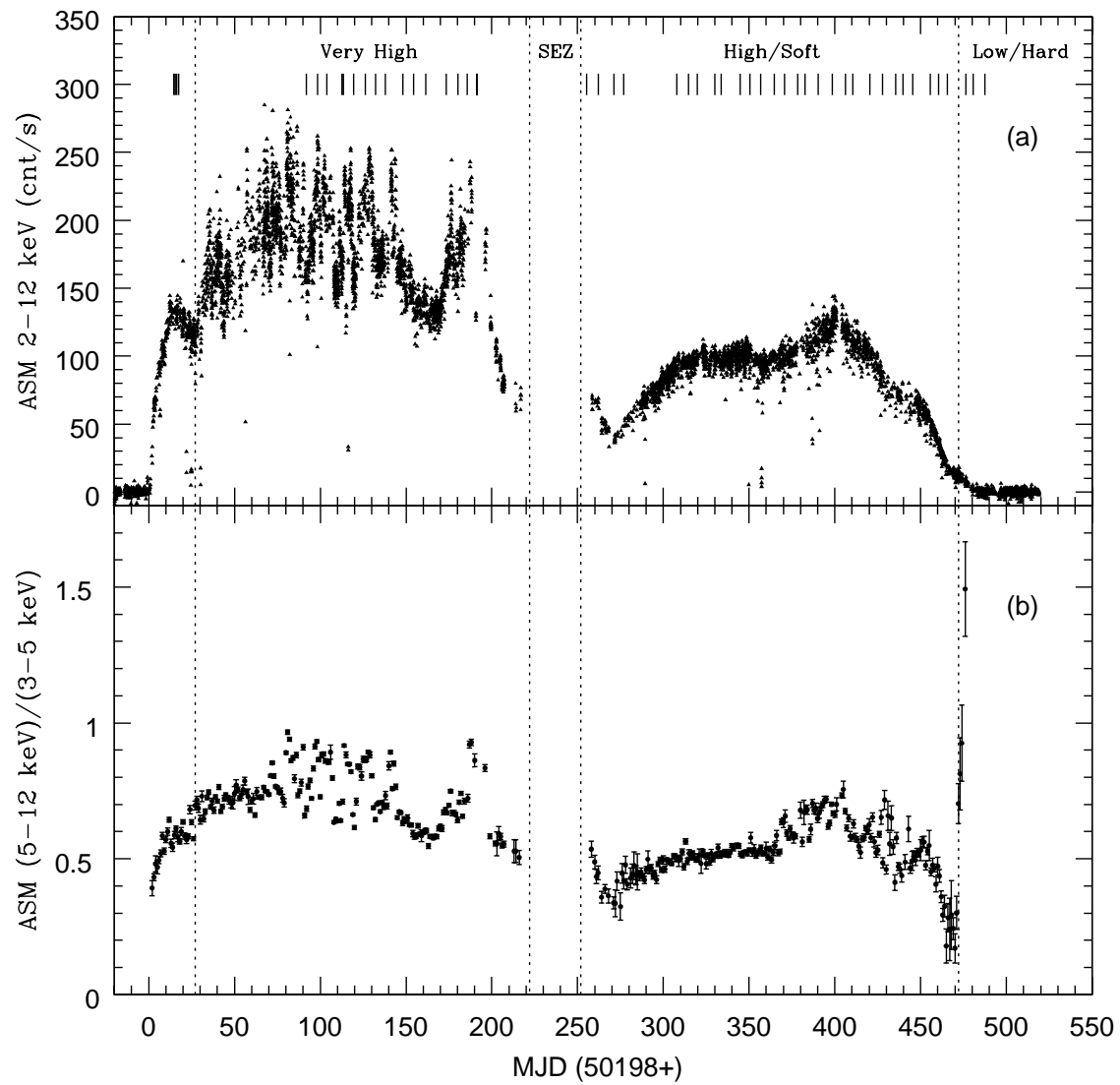


Fig. 1.—

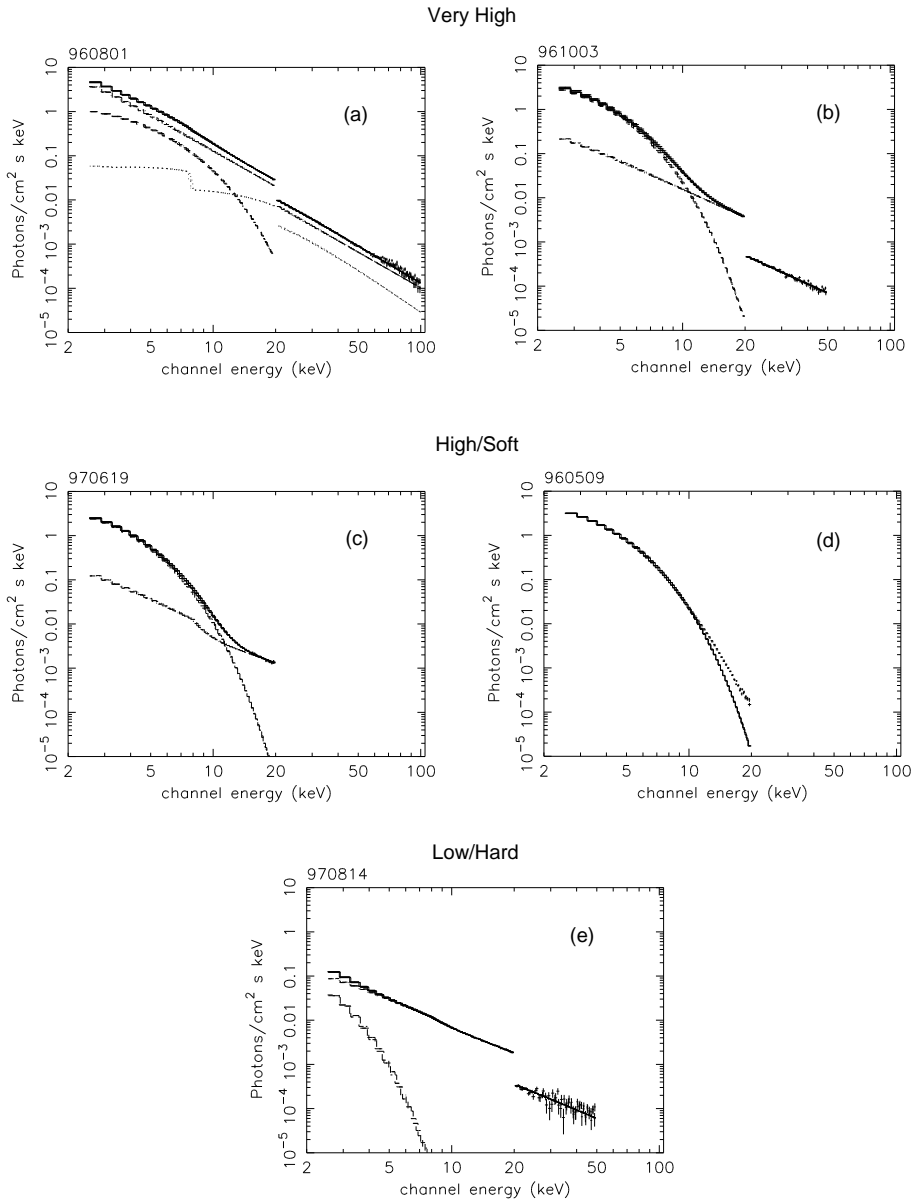


Fig. 2.—

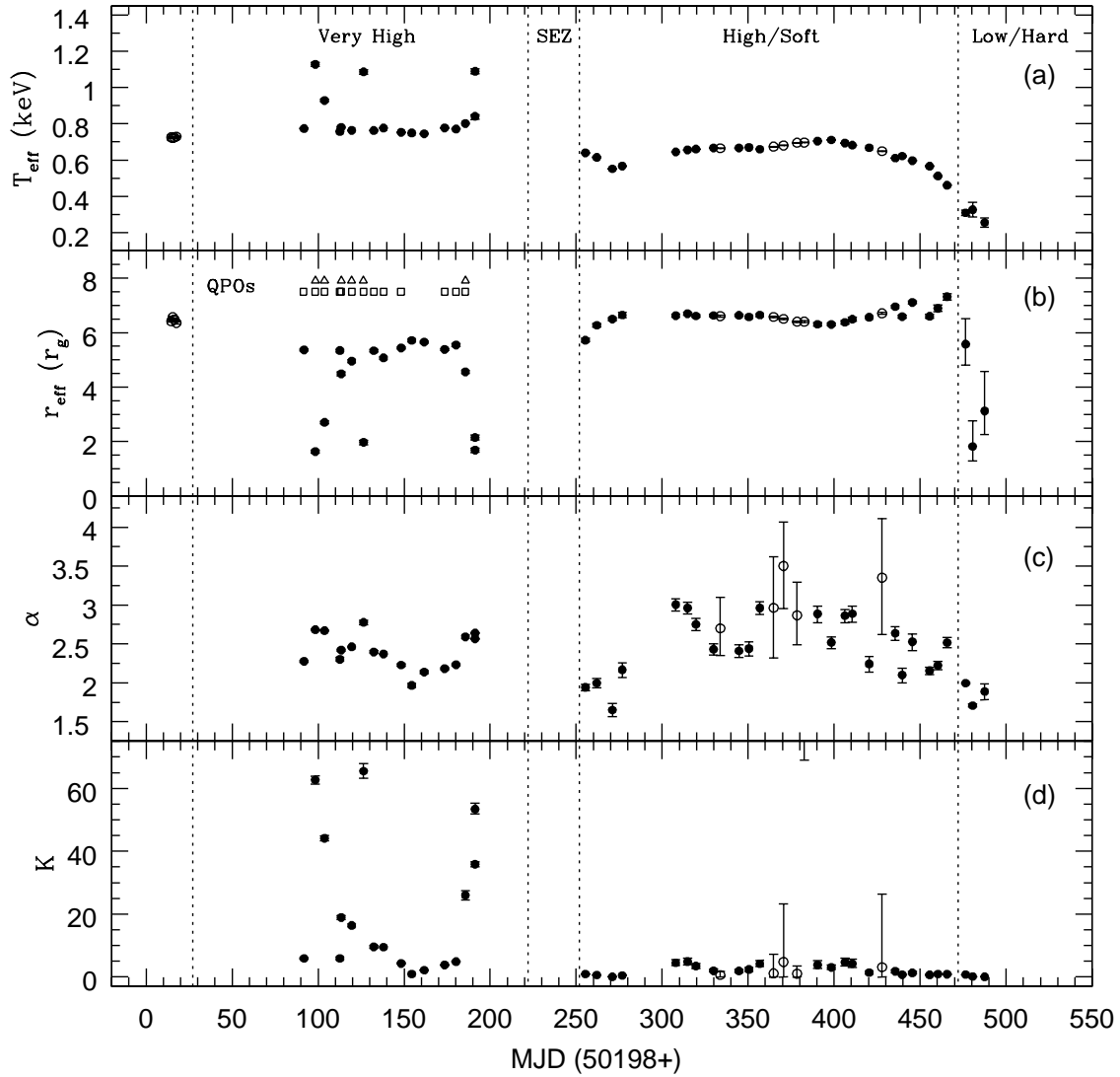


Fig. 3.—

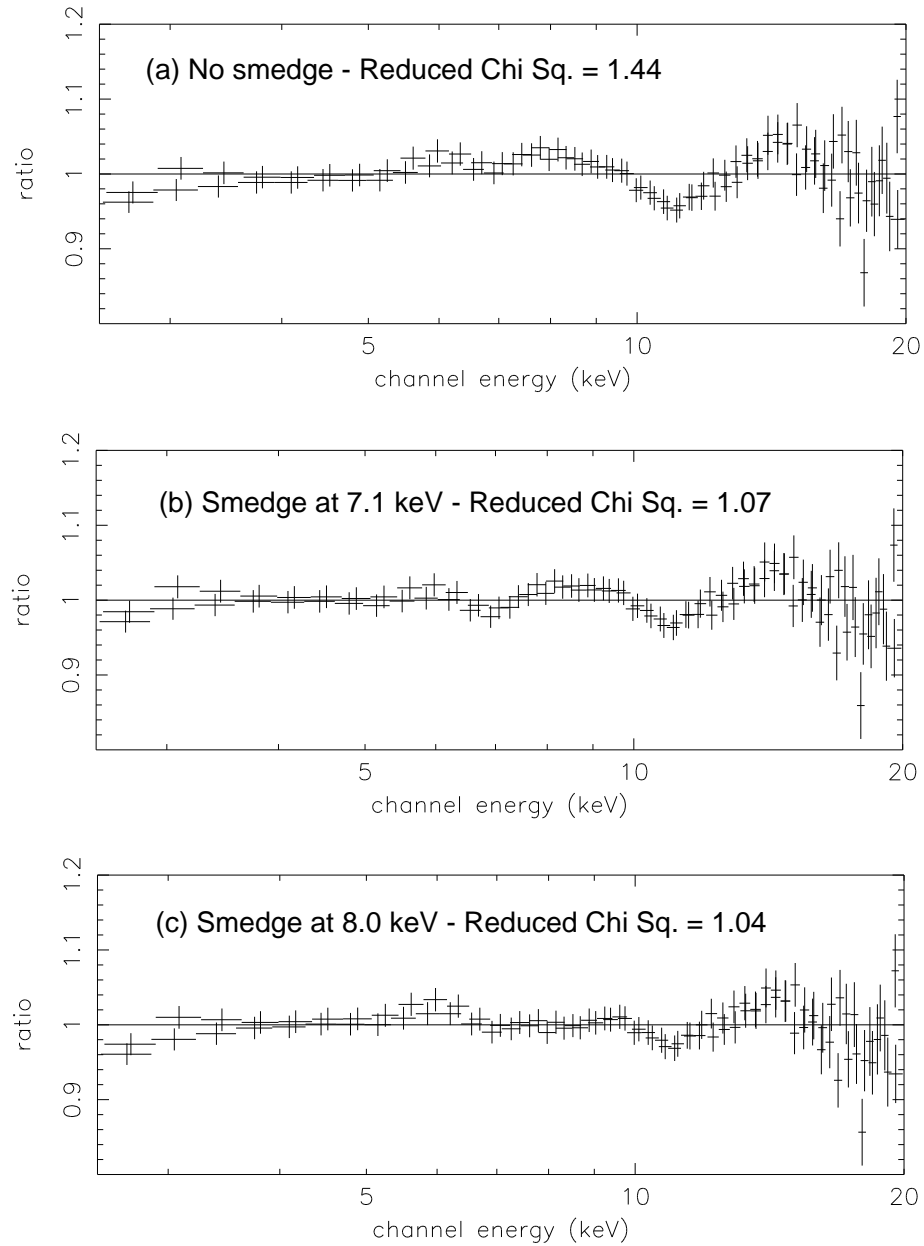


Fig. 4.—

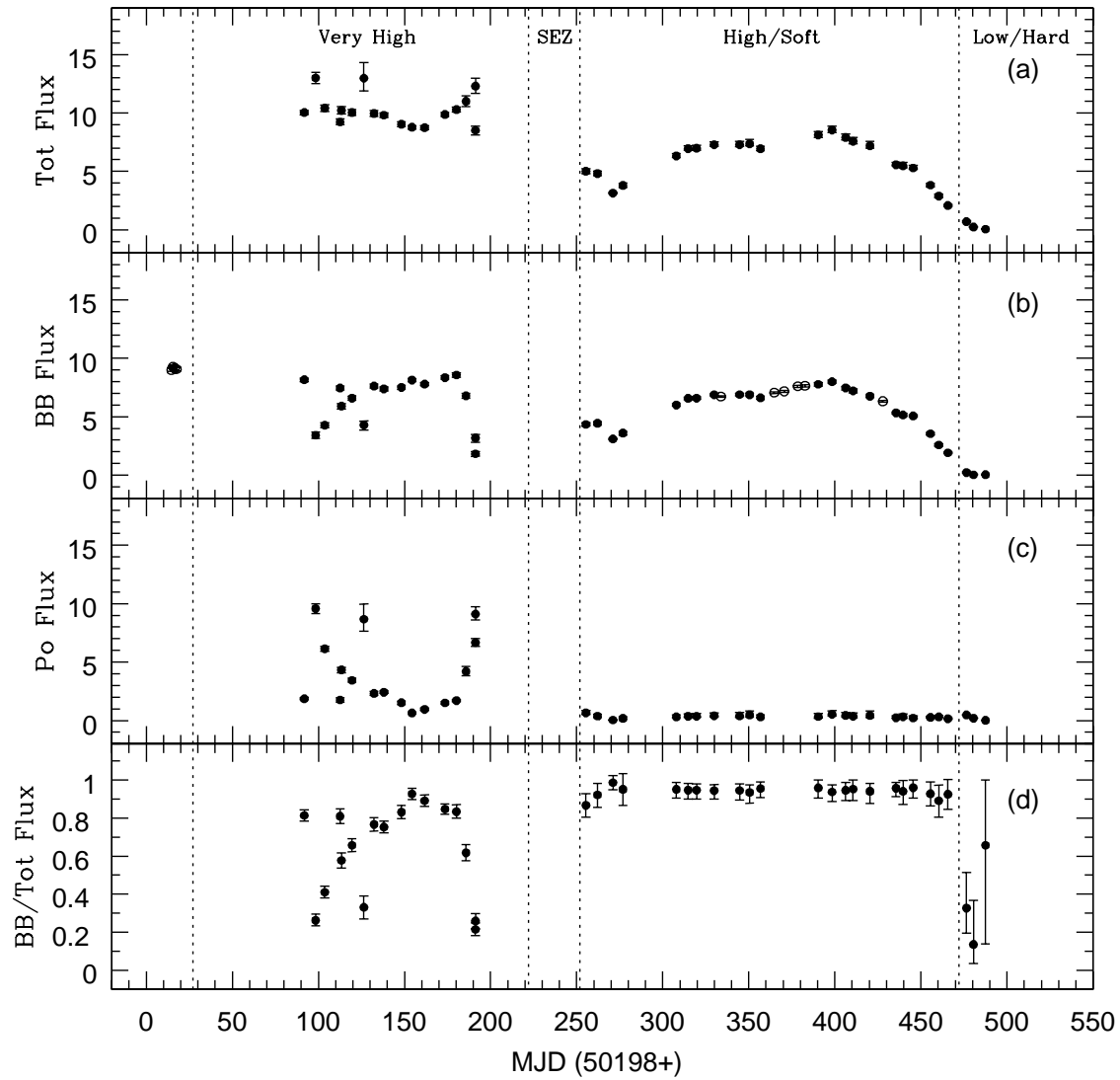


Fig. 5.—

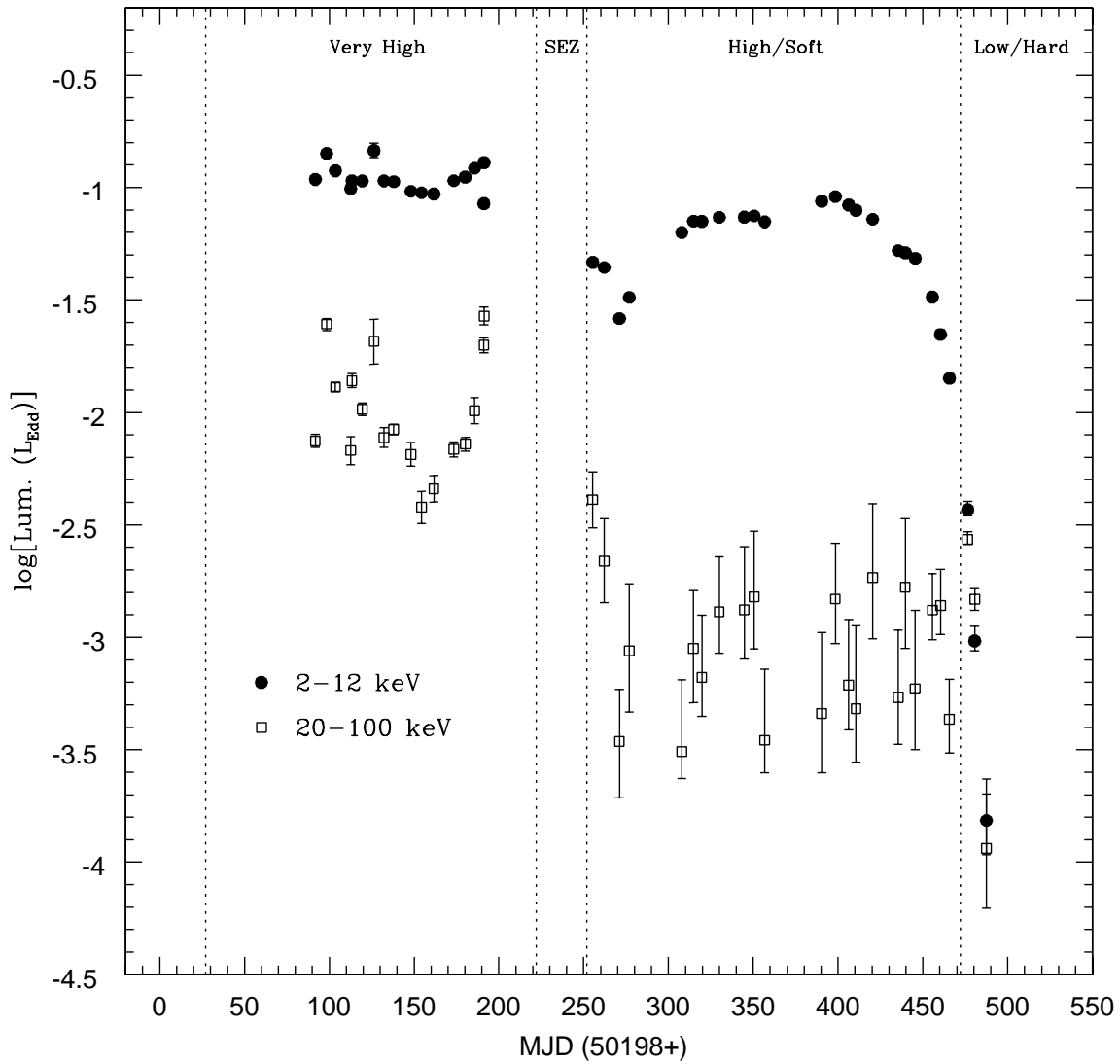


Fig. 6.—

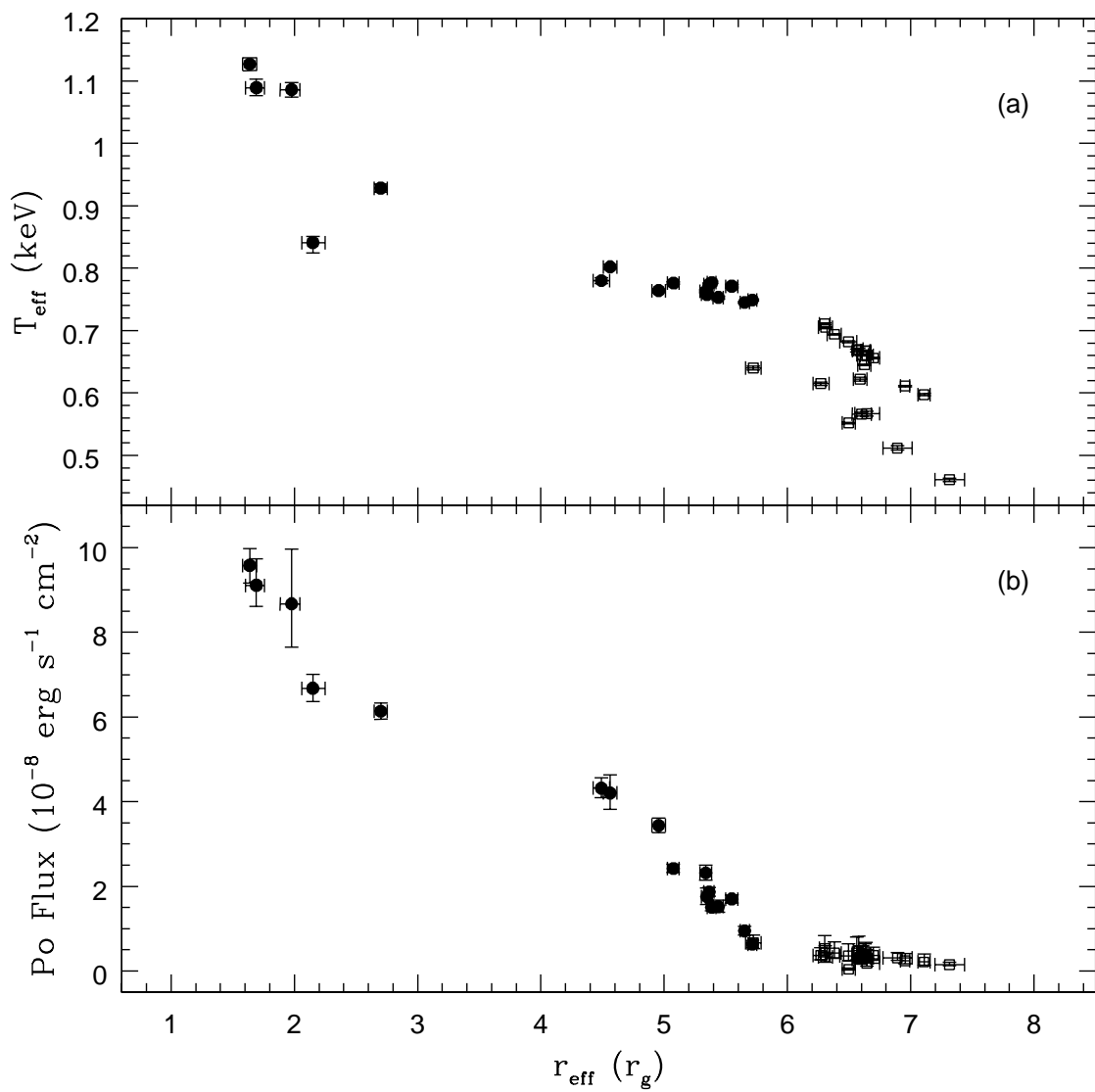


Fig. 7.—

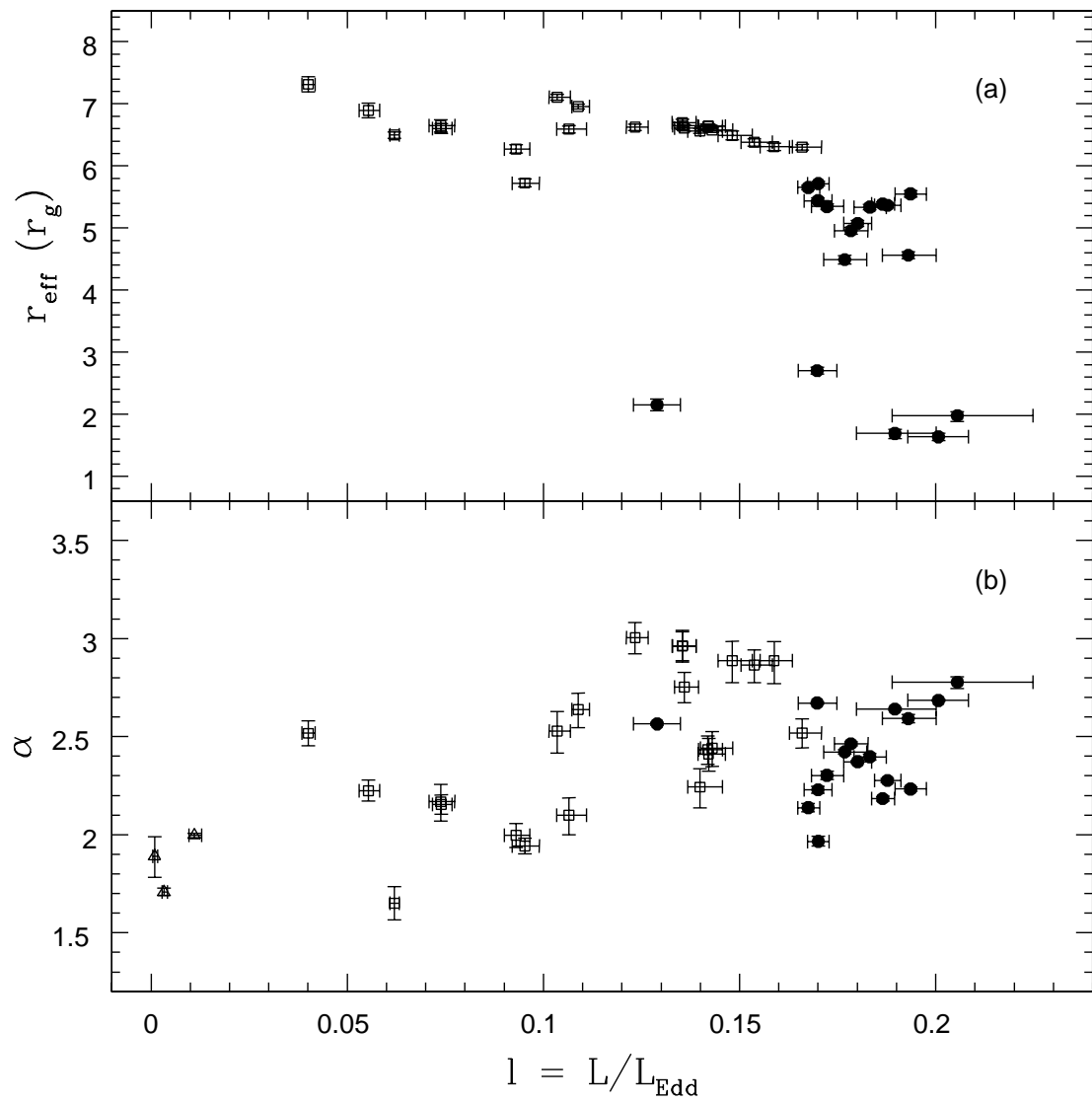


Fig. 8.—

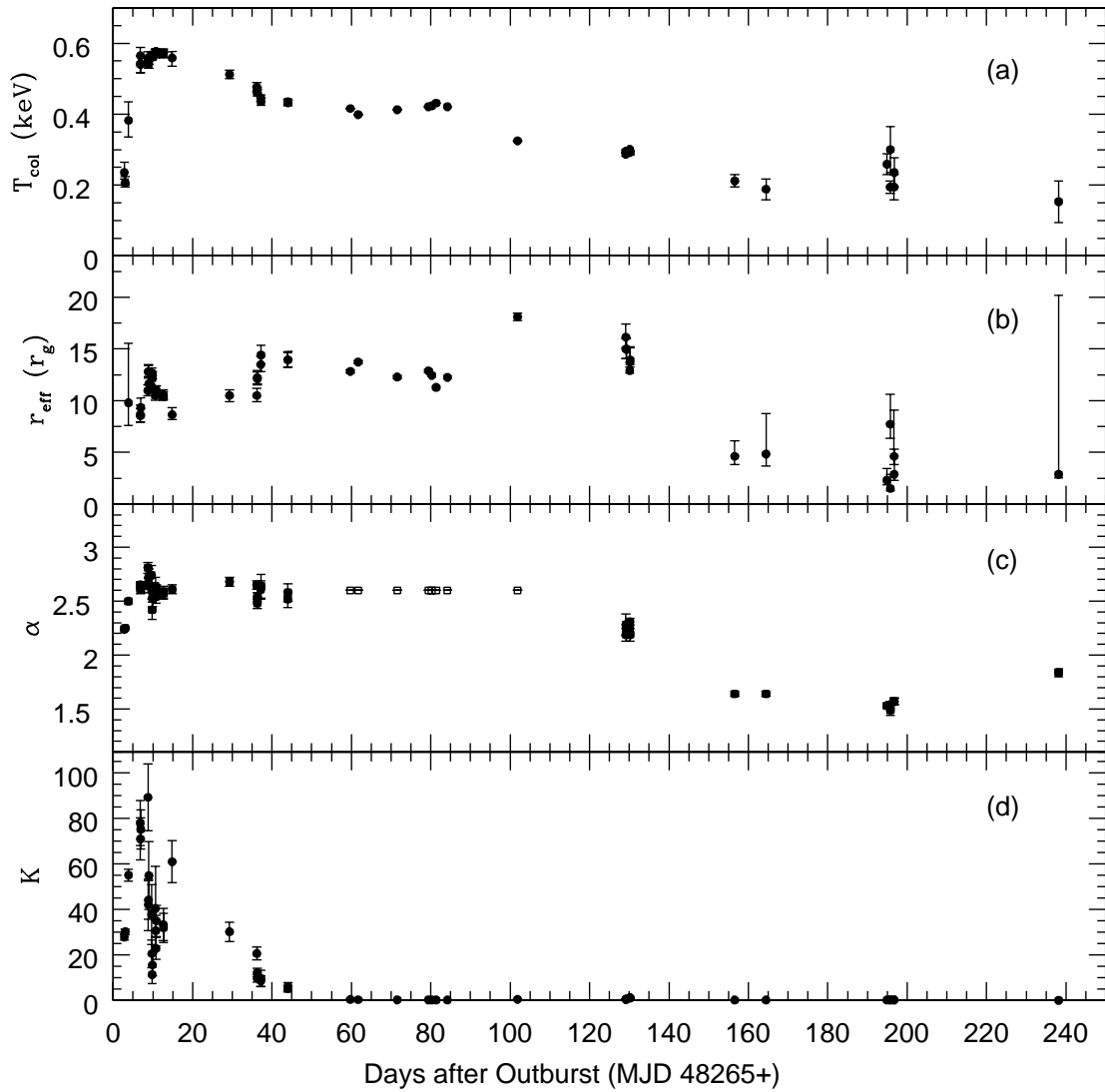


Fig. 9.—

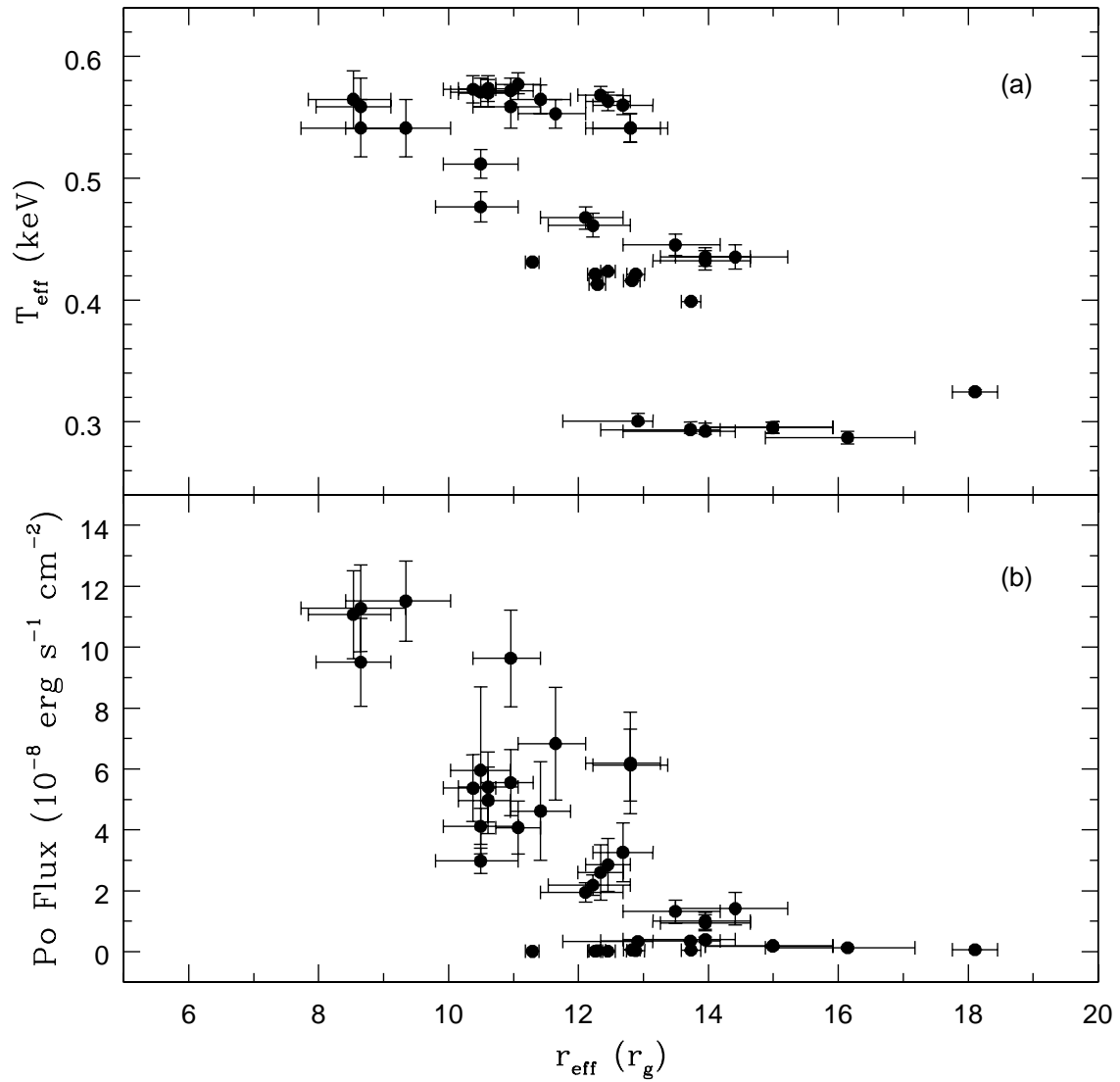


Fig. 10.—

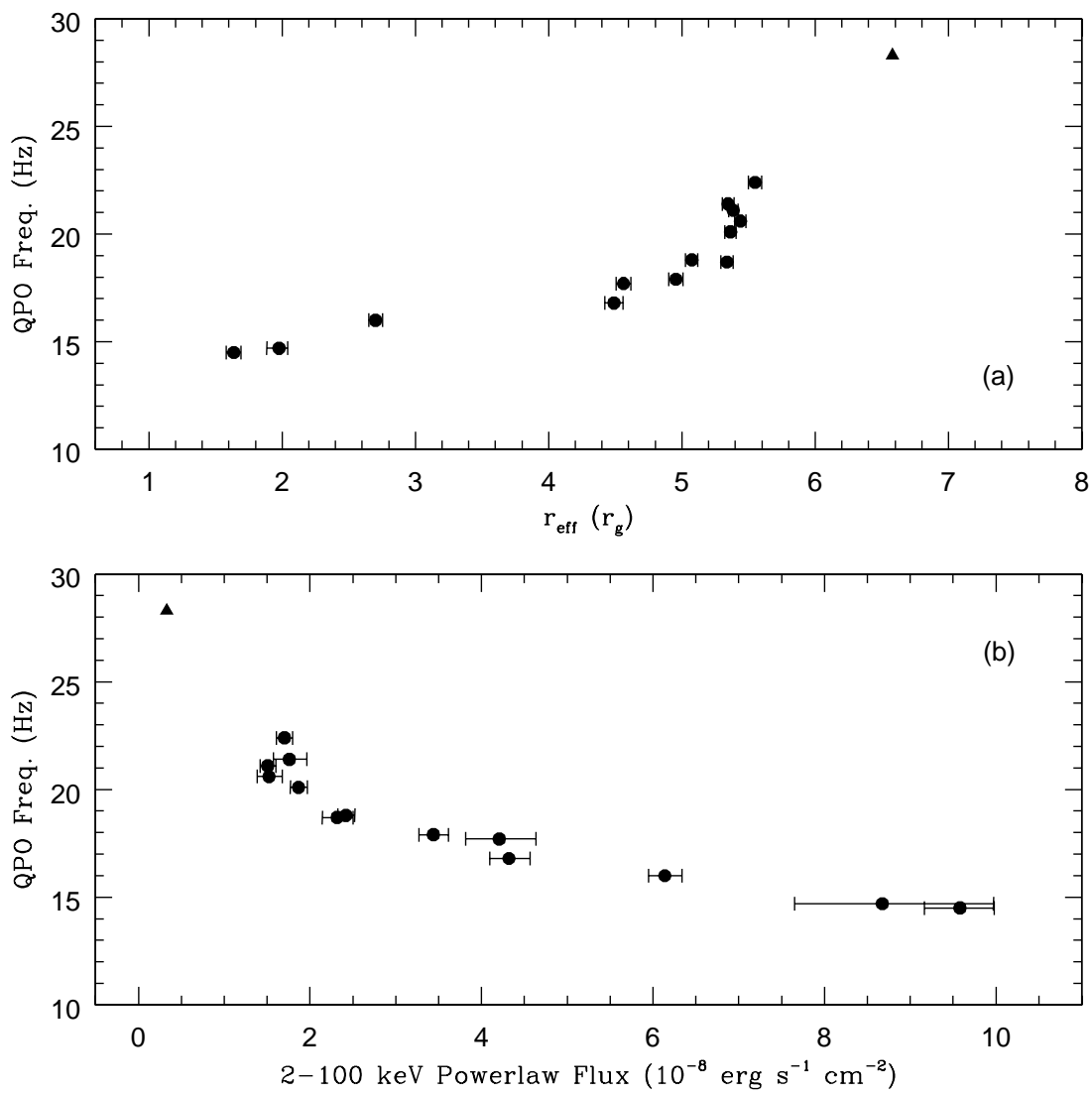


Fig. 11.—